

# Neutron-neutron scattering length from $\pi^+$ photoproduction on the deuteron

Satoshi X. Nakamura,<sup>1,2</sup> Takatsugu Ishikawa,<sup>3</sup> and Toru Sato<sup>4</sup>

<sup>1</sup>*State Key Laboratory of Particle Detection and Electronics, University of Science and Technology of China, Hefei 230036, China*

<sup>2</sup>*Department of Modern Physics, University of Science and Technology of China, Hefei 230026, China*

<sup>3</sup>*Research Center for Electron Photon Science (ELPH), Tohoku University, Sendai 982-0826, Japan*

<sup>4</sup>*Research Center for Nuclear Physics (RCNP), Osaka University, Ibaraki 567-0047, Japan*

## Abstract

We discuss the possibility of extracting the neutron-neutron scattering length  $a_{nn}$  and effective range  $r_{nn}$  from cross section data ( $d^2\sigma/dM_{nn}/d\Omega_\pi$ ), as a function of the  $nn$  invariant mass  $M_{nn}$ , for  $\pi^+$  photoproduction on the deuteron ( $\gamma d \rightarrow \pi^+ nn$ ). The analysis is based on a  $\gamma d \rightarrow \pi^+ nn$  reaction model in which realistic elementary amplitudes for  $\gamma p \rightarrow \pi^+ n$ ,  $NN \rightarrow NN$ , and  $\pi N \rightarrow \pi N$  are built in. We show that  $M_{nn}$  dependence (lineshape) of a ratio  $R_{\text{th}}$ ,  $d^2\sigma/dM_{nn}/d\Omega_\pi$  normalized by  $d\sigma/d\Omega_\pi$  for  $\gamma p \rightarrow \pi^+ n$  and the nucleon momentum distribution inside the deuteron, at the kinematics with  $\theta_\pi = 0^\circ$  and  $E_\gamma \sim 250$  MeV is particularly useful for extracting  $a_{nn}$  and  $r_{nn}$  from the corresponding data  $R_{\text{exp}}$ . It is found that  $R_{\text{exp}}$  with 2% error, resolved into the  $M_{nn}$  bin width of 0.04 MeV (corresponding to the  $p_\pi$  bin width of 0.05 MeV/c), can determine  $a_{nn}$  and  $r_{nn}$  with uncertainties of  $\pm 0.21$  fm and  $\pm 0.06$  fm, respectively, for the case of  $a_{nn} = -18.9$  fm and  $r_{nn} = 2.75$  fm. The requirement of such narrow bin widths indicates that the momenta of the incident photon and the emitted  $\pi^+$  have to be measured with high resolutions. This can be achieved by utilizing virtual photons of very small  $Q^2$  from electron scattering at Mainz MAMI facility. The proposed method for determining  $a_{nn}$  and  $r_{nn}$  from  $\gamma d \rightarrow \pi^+ nn$  has a great experimental advantage over the previous one utilizing  $\pi^- d \rightarrow \gamma nn$  for being free from the formidable task of controlling the neutron detection efficiency and its uncertainty.

## I. INTRODUCTION

The charge symmetry (CS) is an important concept to describe many facets of nuclear physics [1, 2]. The CS leads to a consequence that observables are hardly changed when all protons and neutrons in a nuclear system are replaced by neutrons and protons, respectively. For example, excited states of mirror nuclei have identical energy levels and spin-parity assignments. The CS is more generally defined by the invariance under the rotation by  $180^\circ$  about the  $y$ -axis in the isospin space. This rotation corresponds to, at the quark level, the interchange of the  $u$  and  $d$  quarks and, at the hadron level, the interchange of the proton and the neutron, for example.

Within the Standard Model, the CS is broken due to the difference in the  $u$  and  $d$  quark masses and electromagnetic (EM) effects. These elementary effects show up in hadron phenomenology in various ways such as the neutron ( $n$ ) and proton ( $p$ ) mass difference of 1.3 MeV, and a small charge-dependent component of the nuclear force that breaks the CS at the order of a few percents. In terms of hadronic degrees of freedom, the charge-symmetry breaking (CSB) of the nuclear force can be described with a mixing of neutral rho meson ( $\rho^0$ ) and omega meson ( $\omega$ ) in one boson exchange mechanism [2], and the  $n$ - $p$  mass difference. The CSB force could explain experimental observations of CSB such as: 0.7 MeV difference in the binding energies between  ${}^3\text{H}$  and  ${}^3\text{He}$  (mirror nuclei); the difference of analyzing powers  $A_n(\theta_n) \neq A_p(\theta_p)$  at the same angle  $\theta_n = \theta_p$  for  $np$  scattering [3]; the forward-backward asymmetry  $d\sigma/d\Omega_\pi(\theta) \neq d\sigma/d\Omega_\pi(\pi - \theta)$  in the deuteron ( $d$ ) formation reaction emitting a neutral pion ( $np \rightarrow d\pi^0$ ) [4]. A large difference between  $A = 4$  mirror hypernuclei,  ${}^4_\Lambda\text{H}$  and  ${}^4_\Lambda\text{He}$ , has been recently reported in their excitation energies [5, 6]. Possibly, the CSB appears in hypernuclei more strongly than in ordinary nuclei. The full understanding of CSB still remains an open issue in nuclear physics. To reveal the cause of the CSB observed in few-baryon systems, it is critically important to experimentally investigate the difference between the low-energy elementary  $nn$  and  $pp$  scatterings, and that between  $\Lambda n$  and  $\Lambda p$  scatterings.

The low-energy  $NN$  scattering is characterized by the scattering length  $a$  and effective range  $r$  through an effective-range expansion of the  $S$ -wave phase shift  $\delta(p)$ :

$$p \cot \delta(p) = -\frac{1}{a} + \frac{1}{2} r p^2 + O(p^4), \quad (1)$$

where  $p$  denotes the momentum of the nucleon ( $N$ ) in the  $NN$  center-of-mass (CM) frame. It should be noted that a positive (negative)  $a$  value indicates a repulsion (attraction) in this definition. The experimentally obtained  $a$  and  $r$  parameters for the spin-singlet ( ${}^1S_0$ ) states are

$$\begin{cases} a_{nn} = -18.9 \pm 0.4 \text{ fm}, & r_{nn} = 2.75 \pm 0.11 \text{ fm for } nn, \\ a_{np} = -23.74 \pm 0.02 \text{ fm}, & r_{np} = 2.77 \pm 0.05 \text{ fm for } np, \text{ and} \\ a_{pp} = -17.3 \pm 0.4 \text{ fm}, & r_{pp} = 2.85 \pm 0.04 \text{ fm for } pp, \end{cases} \quad (2)$$

where the EM effects have already been corrected. The scattering length  $a_{np}$  in the  $np$  system is significantly different from the other two ( $a_{nn}$  and  $a_{pp}$ ), suggesting a charge independence breaking (CIB). The CSB is significant in the 1.6-fm difference between  $a_{nn}$  and  $a_{pp}$ . While the error of  $a_{nn}$  is predominantly from the statistical uncertainty in the experiments, that of  $a_{pp}$  from the systematic uncertainty of removing the EM effects.

So far, several different values of  $a_{nn}$  ranging from  $-19$  to  $-16$  fm have been reported (see Ref. [7] for a recent review), and a consensus has not been reached on which value is

correct. An experimental difficulty is that an  $nn$  scattering experiment, with which  $a_{nn}$  can be determined directly, is almost impossible because a realistic free neutron target does not exist. Therefore, the main experimental results for  $a_{nn}$  come from two different types of experiments utilizing the final-state  $nn$  interaction (indirect determination): (i) three-body breakup reaction of  $nd \rightarrow nnp$ ; (ii) radiative capture of a stopped negative pion on the deuteron ( $\pi^-d \rightarrow nn\gamma$ ).

For the type (i) experiments, excluding those before 1973,  $a_{nn}$  values have been extracted from the data with the exact solution of Faddeev equation for  $nd \rightarrow nnp$  [8]. Significantly different values of  $a_{nn}$  have been obtained from the same reaction:

$$\begin{cases} a_{nn} = -16.1 \pm 0.4 \text{ fm } (E_n = 25.3 \text{ MeV, } np \text{ detected [9]),} \\ a_{nn} = -18.7 \pm 0.7 \text{ fm } (E_n = 13.0 \text{ MeV, } nnp \text{ detected [10]), and} \\ a_{nn} = -16.5 \pm 0.9 \text{ fm } (E_n = 17.4 \text{ MeV, } p \text{ detected [11]).} \end{cases} \quad (3)$$

The main concern on these results is possibly large three-body force effects. Because details of the three-body force effects have not been well-established yet, the systematic uncertainty associated with them could be rather underestimated.

The type (ii) experiment of  $\pi^-d \rightarrow nn\gamma$  has been considered to be a more reliable method to determine  $a_{nn}$  because only  $nn$  scattering without three-body force effects takes place in the final state. The obtained experimental value is  $a_{nn} = -18.9 \pm 0.4$  fm after including the correction of  $\Delta a_{nn} \sim -0.3$  fm from the magnetic-moment interaction between  $nn$  [12]. The difficulty of experimentally studying  $\pi^-d \rightarrow nn\gamma$  is to detect low-energy neutrons. The efficiency of detecting them depends on their kinetic energies and is very sensitive to a detector threshold measured in the electron-equivalent energy. In Refs. [12, 13], the efficiencies of the detectors were checked at neutron kinetic energies from 5 to 13 MeV using energy-tagged neutrons produced in the  ${}^2\text{H}(d, n){}^3\text{He}$  reaction. However, a direct measurement has not been done for the detection efficiencies around  $\sim 2.4$  MeV at which neutrons affected by the final-state interaction are expected to appear from  $\pi^-d \rightarrow nn\gamma$ . On the theoretical side, a series of earlier works have been conducted based on a phenomenological approach [14], and a dispersion-relation approach [15]. A modernized work has been also made based on the chiral effective field theory [16]. Thanks to the dominance of the Kroll-Ruderman term, the pion photoproduction amplitude is rather well-controlled. It is reported that the main theoretical uncertainty is from the off-shell behavior of the  $nn$  rescattering amplitude.

Meanwhile, another interesting possibility of determining  $a_{nn}$  is to utilize the final-state  $nn$  interaction in the  $\gamma d \rightarrow \pi^+ nn$  reaction. This possibility was pointed out by Lensky *et al.* [17] where this process was studied with chiral perturbation theory. However, their calculation is limited to the energy region very close to the pion production threshold (photon energy up to 20 MeV above the threshold, corresponding to the emitted pion momentum less than 80 MeV/c). It is difficult to experimentally detect such a low-momentum  $\pi^+$  before its decay. On the other hand, let us consider the reaction at an incident photon energy of  $E_\gamma = 200\text{--}300$  MeV. This energy region is between the pion production threshold ( $E_\gamma \sim 150$  MeV) and the excitation energy of the delta baryon ( $\Delta(1232) P_{33}$ ) ( $E_\gamma \sim 340$  MeV), assuming that the quasi-free  $\gamma p \rightarrow \pi^+ n$  reaction occurs on the initial nucleon at rest inside the deuteron. We choose to detect  $\pi^+$ s emitted at  $\theta_\pi \simeq 0^\circ$  from the photon direction, and only the  $\pi^+$ s near the maximum momentum are of interest. In this particular kinematics, the relative momentum of  $nn$  is very low, and  $nn$  are expected to strongly interact with each other. Also this kinematics would efficiently prevent a pion created in

$\gamma N \rightarrow \pi N$  from rescattering on the spectator nucleon. This is because the  $\pi N$  interaction is rather weak at low energies and/or the spectator nucleon is required to have a large momentum which is largely suppressed in the deuteron. This seems an ideal condition to study the low-energy neutron-neutron scattering, thereby determining  $a_{nn}$  and also  $r_{nn}$ .

For extracting  $a_{nn}$  from  $\pi^- d \rightarrow \gamma nn$  or  $\gamma d \rightarrow \pi^+ nn$ , the experimental challenge is to obtain the  $nn$  invariant mass ( $M_{nn}$ ) distribution at  $M_{nn} \sim 2m_n$  with high statistics and high resolution. In this respect, we find a great advantage in  $\gamma d \rightarrow \pi^+ nn$  over  $\pi^- d \rightarrow \gamma nn$  because we can avoid the neutron detection the efficiency of which could significantly increase the systematic uncertainty. We need to detect only  $\pi^+$ s with the momentum of 120–250 MeV/ $c$  once the incident photon energy is known to a sufficient precision. Thus it seems very valuable to analyze  $\gamma d \rightarrow \pi^+ nn$  data and extract  $a_{nn}$  which is independent of and alternative to those from the previous methods using  $\pi^- d \rightarrow \gamma nn$  and  $nd$  scattering data. For extracting  $a_{nn}$  and  $r_{nn}$  from  $\gamma d \rightarrow \pi^+ nn$  data in a controlled manner, we need to put possible theoretical uncertainties under control. Thus, in this work, we use a theoretical model for the  $\gamma d \rightarrow \pi^+ nn$  reaction, and examine the reaction at particular kinematical conditions of  $E_\gamma = 200\text{--}300$  MeV,  $\theta_\pi \sim 0^\circ$ , and  $M_{nn} \sim 2m_n$ . Through the theoretical analysis of  $\gamma d \rightarrow \pi^+ nn$ , we find that the kinematics and the shape of the  $M_{nn}$  distribution are indeed suitable for studying the low-energy  $nn$  scattering. We also assess possible theoretical uncertainties in extracting  $a_{nn}$  and  $r_{nn}$  from the corresponding data. Finally, we conduct a Monte Carlo simulation to extract  $a_{nn}$  and  $r_{nn}$  from data, prepared with different precisions and different  $M_{nn}$  bin widths, and estimate their uncertainties. The present analysis leads to a proposal of an alternative and more reliable method to extract  $a_{nn}$  and  $r_{nn}$ .

The organization of the rest of this paper is as follows. In Sec. II, we discuss our theoretical formalism to study  $\gamma d \rightarrow \pi^+ nn$ . Numerical results are presented and discussed in Sec. III. Sec. IV is devoted to a discussion on experimental strategy of measuring  $\gamma d \rightarrow \pi^+ nn$  with high resolution using virtual photons of very low  $Q^2$  ( $< 0.01$  GeV<sup>2</sup>). Then, a summary follows in Sec. V.

## II. FORMALISM

### A. $\gamma d \rightarrow \pi^+ nn$ reaction model based on the dynamical coupled-channels model

Our starting point to develop a  $\gamma d \rightarrow \pi^+ nn$  reaction model is elementary amplitudes for  $\gamma N \rightarrow \pi N$  and  $\pi N \rightarrow \pi N$  processes. Here, we employ the elementary amplitudes generated by a dynamical coupled-channels (DCC) model [18, 19]. The DCC model includes meson-baryon channels relevant to the nucleon resonance and  $\Delta$  resonance (generically referred to as  $N^*$ ) region such as  $\pi N, \eta N, K\Lambda, K\Sigma$ , and also  $\pi\Delta, \sigma N, \rho N$  that couple to  $\pi\pi N$ ;  $\gamma^{(*)}N$  channel is also considered perturbatively. The meson-baryon interaction potentials are comprised of meson-exchange non-resonant and (bare)  $N^*$ -excitation resonant mechanisms. The gauge invariance is satisfied at the tree level. By solving the coupled-channel Lippmann-Schwinger equation exactly with off-shell effects fully taken into account, the unitary DCC amplitudes are obtained. The DCC model has been developed through a comprehensive analysis of  $\pi N, \gamma N \rightarrow \pi N, \eta N, K\Lambda, K\Sigma$  data in the CM energy ( $W$ ) region from the channel thresholds to  $W \lesssim 2.1$  GeV. The model gives a reasonable description of the data included in the fits, and the properties of all the well-established nucleon resonances have been extracted from the obtained amplitudes. The DCC model has been extended to a finite  $Q^2$  region by analyzing electron-induced data [20], and also to neutrino-induced

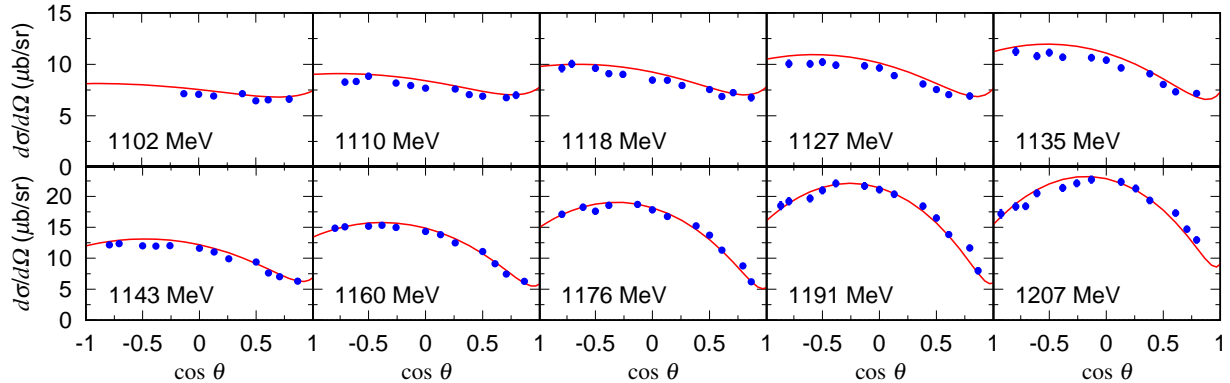


FIG. 1. Differential cross sections for  $\gamma p \rightarrow \pi^+ n$  from the DCC model. The total energy  $W$  is indicated in each panel. The energy  $W = 1121, 1162,$  and  $1201$  MeV corresponds to the incident photon energy of  $E_\gamma \simeq 200, 250,$  and  $300$  MeV, respectively. The data are taken from Ref. [23]. The errors shown are statistical only.

reactions by developing the axial current amplitudes [20–22].

The  $\gamma p \rightarrow \pi^+ n$  elementary amplitude is of primary importance in developing a  $\gamma d \rightarrow \pi^+ nn$  model. Therefore, it is reassuring to see in Fig. 1 that the DCC model well describes  $\gamma p \rightarrow \pi^+ n$  cross section data in the energy region relevant to this work. However, data are unavailable for the forward direction ( $\cos \theta = 1$ ) which is particularly important for our purpose. Also, the data shown in Fig. 1 additionally have systematic errors. These facts may worry the readers if we can develop a  $\gamma d \rightarrow \pi^+ nn$  model that reaches a precision required to extract  $a_{nn}$  from data. As we will discuss later, when extracting  $a_{nn}$ , we use a method to largely cancel out the normalization uncertainty of the elementary  $\gamma p \rightarrow \pi^+ n$  amplitudes.

With the DCC model as the starting point, it is straightforward to extend the model to a  $\pi NN$  system following the well-established multiple scattering theory [24]. In this work, we consider the impulse and first-order rescattering terms as depicted in Fig. 2, where higher order rescattering terms are truncated. This setup including up to the first-order rescattering has been often used in the literatures [25–31], and has been shown to provide reasonable description of  $\gamma d \rightarrow \pi NN$  data with significant rescattering effects. As we will see, this truncation is a good approximation for the particular kinematics considered in this work.

Similar DCC-based deuteron reaction models have been successfully applied to several problems of current interest. We proposed a novel method to determine the  $\eta N$  scattering length using  $\gamma d \rightarrow \eta pn$  data at a special kinematics in Ref. [32]. In Ref. [33], the extraction of neutron-target observables from  $\gamma d \rightarrow \pi NN$  data was examined, and some rescattering effects observed in the data are well explained for the first time. Ref. [34] corrected the neutrino-nucleon cross sections from neutrino-deuteron data by estimating the rescattering effects, significantly contributing to the neutrino oscillation experiments [35].

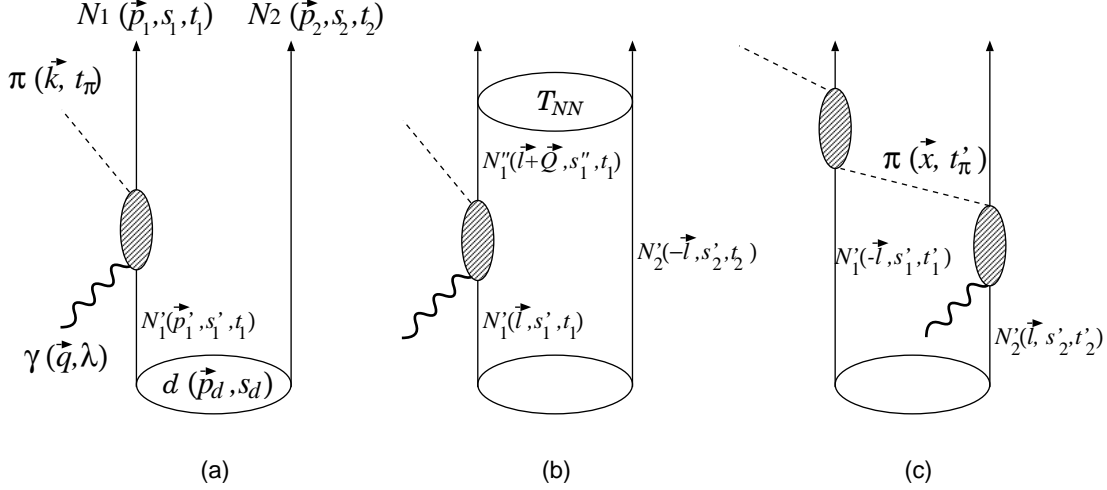


FIG. 2. Diagrams for  $\gamma d \rightarrow \pi^+ nn$  considered in this work. (a) impulse, (b)  $NN$  rescattering, and (c)  $\pi N$  rescattering mechanisms. We introduce  $\mathbf{Q} \equiv \mathbf{q} - \mathbf{k}$  and  $\mathbf{x} \equiv \mathbf{q} - \mathbf{p}_2 + \mathbf{l}$ . The shaded ellipses are elementary amplitudes from the dynamical coupled-channels model.

## B. Cross section formula

The unpolarized differential cross section formula for  $\gamma(\mathbf{q}) + d(\mathbf{p}_d) \rightarrow \pi^+(\mathbf{k}) + n_1(\mathbf{p}_1) + n_2(\mathbf{p}_2)$  in the laboratory frame ( $\mathbf{p}_d = 0$ ) is given as

$$\frac{d^2\sigma(E_\gamma)}{d\Omega_{\mathbf{k}} dM_{nn}} = \frac{1}{6} \sum_{\lambda, s_d} \sum_{s_1, s_2} \frac{(2\pi)^4}{4E_\gamma} \frac{1}{2E_d(\mathbf{p}_d)} \int d\Omega_{\mathbf{p}_{nn}} \frac{p_{nn} k^2 m_n^2}{|kE - \mathbf{q} \cdot \hat{\mathbf{k}} E_\pi(\mathbf{k})|} |M(E)|^2, \quad (4)$$

where  $\lambda$  is the photon polarization and  $s_d$  ( $s_i$ ) the  $z$ -component of the deuteron (neutron  $i$ ) spin, and the factor of  $1/6$  for averaging the initial spins. The energy  $E_x$  for a particle  $x$  depends on the particle mass ( $m_x$ ) and momentum ( $\mathbf{p}_x$ ) as  $E_x = \sqrt{\mathbf{p}_x^2 + m_x^2}$ , and the total energy in the laboratory frame is  $E = m_d + E_\gamma$ . The  $\mathbf{p}_{nn}$  denotes the momentum of a neutron in the  $n_1 n_2$  CM frame. We simply write the magnitudes of the momenta as  $k \equiv |\mathbf{k}|$  and  $\hat{k} \equiv \mathbf{k}/|\mathbf{k}|$ . The quantity  $M(E)$  is the Lorentz-invariant amplitude that will be defined below.

As discussed in subsection II A, we describe the  $\gamma d \rightarrow \pi^+ nn$  reaction by considering the impulse [ $t_{\text{imp}}$ , Fig. 2(a)],  $NN$  rescattering [ $t_{NN}$ , Fig. 2(b)], and  $\pi N$  rescattering [ $t_{\pi N}$ , Fig. 2(c)] mechanisms. The corresponding amplitudes are written with the kinematical

variables defined in Fig. 2 as (see Ref. [31] for a more detailed discussion)

$$t_{\text{imp}} = \sqrt{2} \sum_{s'_1, t'_1} \langle \pi(\mathbf{k}, t_\pi) N_1(\mathbf{p}_1, s_1, t_1) | t_{\pi N, \gamma N}(M_{\pi N_1}) | \gamma(\mathbf{q}, \lambda) N'_1(-\mathbf{p}_2, s'_1, t'_1) \rangle \\ \times \langle N'_1(-\mathbf{p}_2, s'_1, t'_1) N_2(\mathbf{p}_2, s_2, t_2) | \Psi_d(s_d) \rangle , \quad (5)$$

$$t_{NN} = \sqrt{2} \sum_{s'_1, \tilde{s}'_1, s'_2, t'_1} \int d\mathbf{l} \\ \times \langle N_1(\mathbf{p}_1, s_1, t_1) N_2(\mathbf{p}_2, s_2, t_2) | t_{NN, NN}(M_{N_1 N_2}) | \tilde{N}'_1(\mathbf{q} - \mathbf{k} + \mathbf{l}, \tilde{s}'_1, t_1) N'_2(-\mathbf{l}, s'_2, t_2) \rangle \\ \times \frac{\langle \pi(\mathbf{k}, t_\pi) \tilde{N}'_1(\mathbf{q} - \mathbf{k} + \mathbf{l}, \tilde{s}'_1, t_1) | t_{\pi N, \gamma N}(W) | \gamma(\mathbf{q}, \lambda) N'_1(\mathbf{l}, s'_1, t'_1) \rangle}{E - E_N(\mathbf{q} - \mathbf{k} + \mathbf{l}) - E_N(-\mathbf{l}) - E_\pi(\mathbf{k}) + i\epsilon} \\ \times \langle N'_1(\mathbf{l}, s'_1, t'_1) N'_2(-\mathbf{l}, s'_2, t_2) | \Psi_d(s_d) \rangle , \quad (6)$$

$$t_{\pi N} = \sqrt{2} \sum_{s'_1, s'_2, t'_1, t'_2, t'_\pi} \int d\mathbf{l} \langle \pi(\mathbf{k}, t_\pi) N_1(\mathbf{p}_1, s_1, t_1) | t_{\pi N, \pi N}(M_{\pi N_1}) | \pi(\mathbf{q} - \mathbf{p}_2 + \mathbf{l}, t'_\pi) N'_1(-\mathbf{l}, s'_1, t'_1) \rangle \\ \times \frac{\langle \pi(\mathbf{q} - \mathbf{p}_2 + \mathbf{l}, t'_\pi) N_2(\mathbf{p}_2, s_2, t_2) | t_{\pi N, \gamma N}(W) | \gamma(\mathbf{q}, \lambda) N'_2(\mathbf{l}, s'_2, t'_2) \rangle}{E - E_N(\mathbf{p}_2) - E_N(-\mathbf{l}) - E_\pi(\mathbf{q} - \mathbf{p}_2 + \mathbf{l}) + i\epsilon} \\ \times \langle N'_1(-\mathbf{l}, s'_1, t'_1) N'_2(\mathbf{l}, s'_2, t'_2) | \Psi_d(s_d) \rangle . \quad (7)$$

The exchange terms are obtained from Eqs. (5)–(7) by flipping the overall sign and interchanging all subscripts 1 and 2 for the nucleons in the intermediate and final  $\pi NN$  states. In the above expressions, the deuteron state with spin projection  $s_d$  is denoted as  $|\Psi_d(s_d)\rangle$ ;  $|N(\mathbf{p}, s, t)\rangle$  the nucleon state with momentum  $\mathbf{p}$  and spin and isospin projections  $s$  and  $t$ ;  $|\gamma(\mathbf{q}, \lambda)\rangle$  the photon state with momentum  $\mathbf{q}$  and polarization  $\lambda$ ;  $|\pi(\mathbf{k}, t_\pi)\rangle$  the pion state with momentum  $\mathbf{k}$  and the isospin projection  $t_\pi$ . The two-body elementary amplitudes depend on the invariant masses that are calculated according to the spectator approximation as

$$M_{\pi N_1} = \sqrt{[E_\pi(\mathbf{k}) + E_N(\mathbf{p}_1)]^2 - (\mathbf{k} + \mathbf{p}_1)^2} , \quad (8)$$

$$M_{N_1 N_2} = \sqrt{[E_N(\mathbf{p}_1) + E_N(\mathbf{p}_2)]^2 - (\mathbf{p}_1 + \mathbf{p}_2)^2} , \quad (9)$$

$$W = \sqrt{[E - E_N(-\mathbf{l})]^2 - (\mathbf{l} + \mathbf{q})^2} . \quad (10)$$

The two-nucleon energy in the propagator of the  $NN$  rescattering amplitude in Eq. (6) is calculated with a non-relativistic approximation:

$$E_N(\mathbf{q} - \mathbf{k} + \mathbf{l}) + E_N(-\mathbf{l}) \simeq \sqrt{(2m_N)^2 + (\mathbf{q} - \mathbf{k})^2} + \frac{(\mathbf{q}/2 - \mathbf{k}/2 + \mathbf{l})^2}{m_N} . \quad (11)$$

Finally, the Lorentz-invariant scattering amplitude  $[M(E)]$  used in Eq. (4) is expressed with the amplitudes of Eqs. (5)–(7) by

$$M(E) = \sqrt{\frac{8E_\gamma E_d(\mathbf{p}_d) E_\pi(\mathbf{k}) E_n(\mathbf{p}_1) E_n(\mathbf{p}_2)}{m_n^2}} \\ \times \left( t_{\text{imp}}(E) + t_{NN}(E) + t_{\pi N}(E) + \{\text{exchange terms}\} \right) . \quad (12)$$

Regarding the off-shell elementary amplitudes used in Eqs. (5)–(7), we use those generated by the DCC model for the pion photoproduction amplitudes ( $t_{\pi N, \gamma N}$ ) and pion-nucleon scattering amplitudes ( $t_{\pi N, \pi N}$ ). For the half off-shell  $NN$  scattering amplitudes ( $t_{NN, NN}$ ) and the deuteron wave function ( $\Psi_d$ ), we use high-precision phenomenological  $NN$  potentials to generate them.

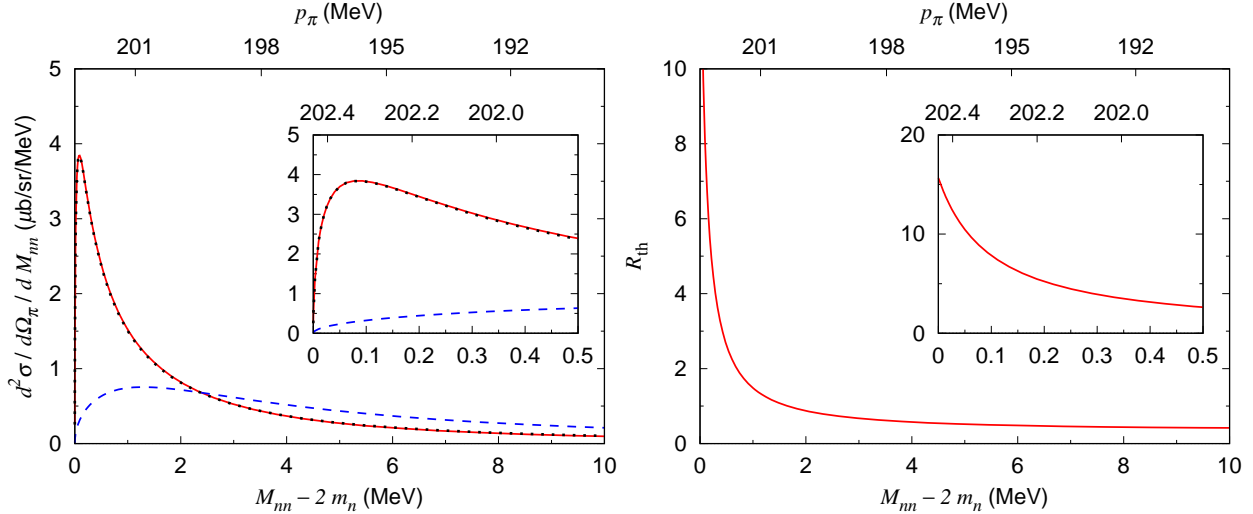


FIG. 3. (Left)  $nn$  invariant mass ( $M_{nn}$ ) distribution for  $\gamma d \rightarrow \pi^+ nn$ . The incident photon energy is  $E_\gamma = 250$  MeV, and the pion emission angle is fixed at  $\theta_\pi = 0^\circ$ . The blue dashed, black dotted, and red solid curves are calculated with the impulse, impulse +  $NN$  rescattering, and impulse +  $NN$  +  $\pi N$  rescattering mechanisms, respectively. The emitted pion momentum is indicated on the upper horizontal axis. The inset shows the small  $M_{nn}$  region. (Right) Ratio  $R_{\text{th}}$  defined in Eq. (13) for the same condition as the left panel.

### III. RESULTS AND DISCUSSION

We show in Fig. 3(left) the neutron-neutron invariant mass ( $M_{nn}$ ) distribution ( $d^2\sigma/dM_{nn}/d\Omega_\pi$  as a function of  $M_{nn}$ ) for  $\gamma d \rightarrow \pi^+ nn$  at  $E_\gamma = 250$  MeV, calculated with three sets of the mechanisms: the impulse mechanism, the impulse +  $NN$  rescattering mechanisms, and the impulse +  $NN$  +  $\pi N$  rescattering mechanisms. Here, we use the CD-Bonn potential [36] to describe the  $NN$  rescattering and the deuteron wave function. The pion emission angle is fixed at  $\theta_\pi = 0^\circ$ . We focus on a small  $M_{nn}$  region since we are interested in the neutron-neutron scattering in this region. The impulse contribution has a quasi-free peak at  $M_{nn} - 2m_n \sim 1.3$  MeV. In this particular kinematics, the  $NN$  rescattering contribution is very large and creates a sharp peak at  $M_{nn} \sim 2m_n$ . This is due to the strong  $NN$  interaction in the  $^1S_0$  wave at low energies. On the other hand, we see that the  $\pi N$  rescattering contribution hardly changes the cross sections. This indicates that the pion is well separated from the  $nn$  system in this kinematics, and thus multiple scattering effects beyond the first-order rescattering is negligibly small. Thus this is a favorable kinematics for our model that considers the diagrams in Fig. 2.

Now we introduce a ratio  $R_{\text{th}}$  defined by

$$R_{\text{th}} = \left[ \frac{d^2\sigma(E_\gamma)}{d\Omega_{\mathbf{k}}dM_{nn}} \right] \bigg/ \left[ \frac{d^2\sigma_{\text{conv}}(E_\gamma)}{d\Omega_{\mathbf{k}}dM_{nn}} \right], \quad (13)$$

where the numerator is given in Eq. (4) and it includes the impulse +  $NN$  +  $\pi N$  rescattering mechanisms. The denominator is defined by

$$\frac{d^2\sigma_{\text{conv}}(E_\gamma)}{d\Omega_{\mathbf{k}}dM_{nn}} = \frac{d\sigma_{\gamma p \rightarrow \pi^+ n}(E_\gamma)}{d\Omega_{\mathbf{k}}} \int d^3p_s \frac{m_n}{E_n(p_s)} |\Psi_d(p_s)|^2 \delta(M_{nn} - \mathcal{M}_{nn}(\mathbf{p}_s, E_\gamma)), \quad (14)$$

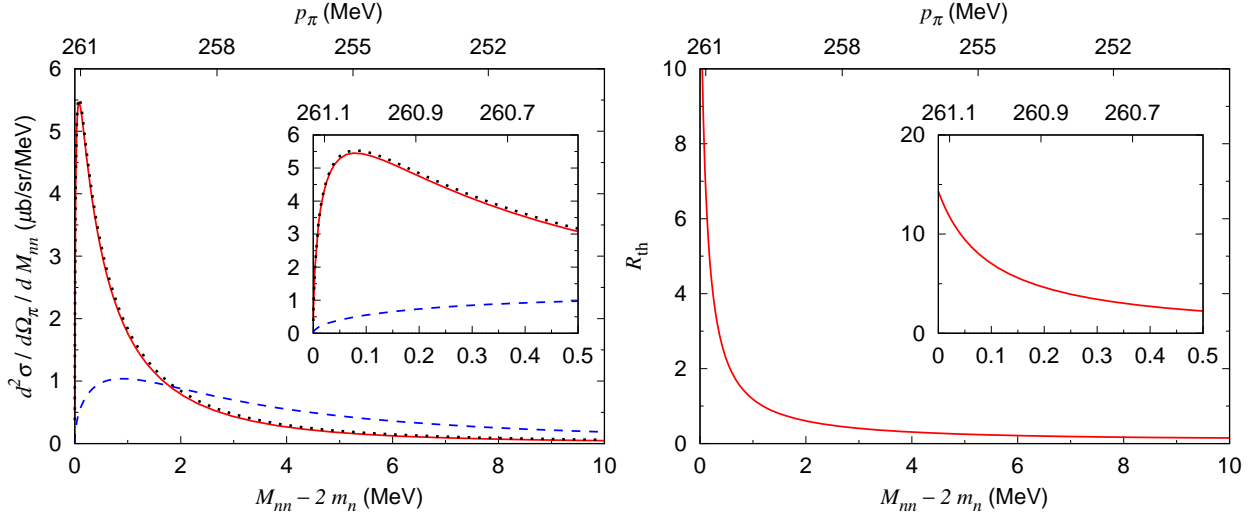


FIG. 4. Same as Fig. 3 but for the incident photon energy of  $E_\gamma = 300$  MeV.

with

$$\mathcal{M}_{nn}(\mathbf{p}_s, E_\gamma) = \sqrt{(E_n(\mathbf{q} - \mathbf{k} - \mathbf{p}_s) + E_n(\mathbf{p}_s))^2 - (\mathbf{q} - \mathbf{k})^2}, \quad (15)$$

and  $d\sigma_{\gamma p \rightarrow \pi^+ n}/d\Omega_{\mathbf{k}}$  is the differential cross sections for  $\gamma p \rightarrow \pi^+ n$  in the laboratory frame. Eq. (14) can be derived from Eq. (4) with prescriptions: (i) consider the impulse mechanism only; (ii) use the  $\gamma p \rightarrow \pi^+ n$  amplitudes assuming that the initial proton is at rest and free (without binding energy) inside the deuteron; (iii) ignore the interference with the exchange term; (iv) ignore the deuteron  $d$ -wave contribution. The deviation of  $R_{\text{th}}$  from 1 is a rough measure of the rescattering effects. The practical advantage of using  $R_{\text{th}}$  over using the cross section itself is that the overall normalization uncertainty of the  $\gamma p \rightarrow \pi^+ n$  amplitudes is largely canceled in  $R_{\text{th}}$ . This uncertainty is mainly a carry-over from those in the  $\gamma p \rightarrow \pi^+ n$  data fitted. The use of the ratio is also advantageous from an experimental viewpoint because the counterpart  $R_{\text{exp}}$  is given with measurable cross sections of proton and deuteron targets and the deuteron wave function; the systematic uncertainty in the overall normalization associated with the number of incident particles, the target thickness, and the solid angle for the pion detection is also largely canceled in  $R_{\text{exp}}$ . We present  $R_{\text{th}}$  in Fig. 3(right) at the same kinematical setting as the left panel. Again, the strong rescattering effect is clearly observed at  $M_{nn} \sim 2m_n$ .

Next we look at results at different  $E_\gamma$ s. In Fig. 4,  $d^2\sigma/d\Omega_\pi/dM_{nn}$  and  $R_{\text{th}}$  are given for  $E_\gamma = 300$  MeV. While the lineshapes are rather similar to those in Fig. 3, the pion rescattering effect is discernible at this energy. To reduce the theoretical uncertainty, it is safe to avoid kinematics where the pion rescattering effect is non-negligible. The result for  $E_\gamma = 200$  MeV is shown in Fig. 5 which is qualitatively similar to Fig. 3. At low photon energies, one may concern a contribution from the elementary  $\gamma p \rightarrow \pi^+ n$  amplitude in the subthreshold region. When the loop momentum becomes large in the diagrams of Figs. 2(b) and (c),  $W$  for the elementary  $\gamma p \rightarrow \pi^+ n$  amplitude, given by Eq. (10), can be below the  $\pi N$  threshold. We find such a contribution is  $\sim 2\%$  to the  $\gamma d \rightarrow \pi^+ nn$  cross sections. Because the subthreshold amplitude is difficult to control, it is better to use higher  $E_\gamma$  to suppress this contribution. We found that the subthreshold contribution is negligibly small

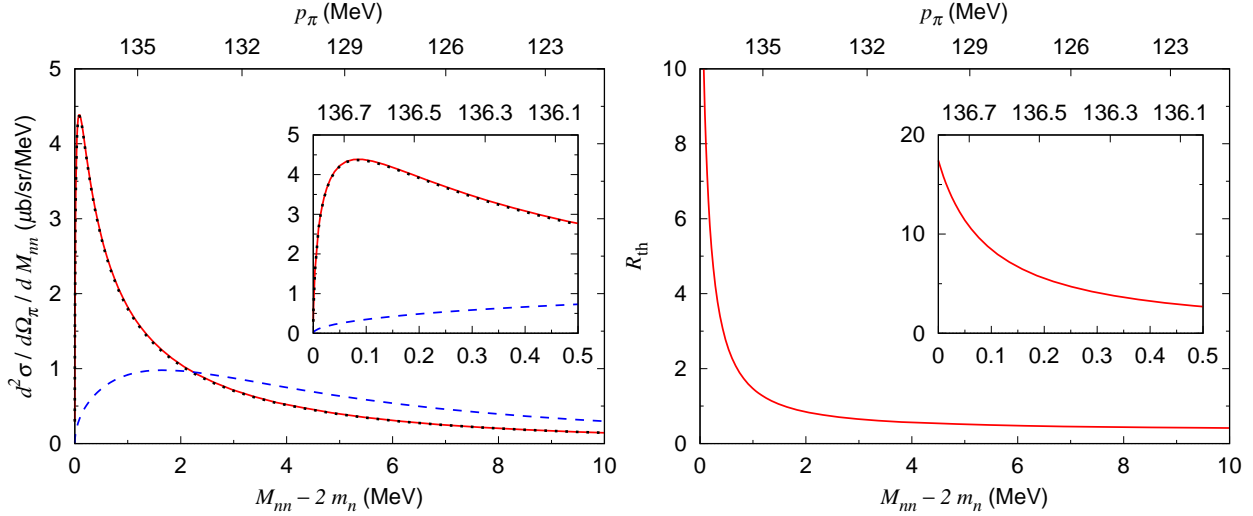


FIG. 5. Same as Fig. 3 but for the incident photon energy of  $E_\gamma = 200$  MeV.

for  $E_\gamma \gtrsim 250$  MeV. Thus, in what follows, we choose to study  $\gamma d \rightarrow \pi^+ nn$  at  $E_\gamma = 250$  MeV.

We examine the pion emission angle dependence of the  $\gamma d \rightarrow \pi^+ nn$  cross section. The  $M_{nn}$  distributions for different angles are shown in Fig. 6. The emission angle is changed from  $0^\circ$  to  $45^\circ$  in the laboratory frame. In the small  $M_{nn}$  region which is the most sensitive to the  $nn$  scattering length, the cross section is significantly larger for smaller emission angle. Thus, from a statistical viewpoint, a small emission angle  $\theta_\pi \sim 0^\circ$  is favorable to measure the cross sections and determine  $a_{nn}$  experimentally. As will be discussed in Sec. IV,  $\theta_\pi = 0^\circ$

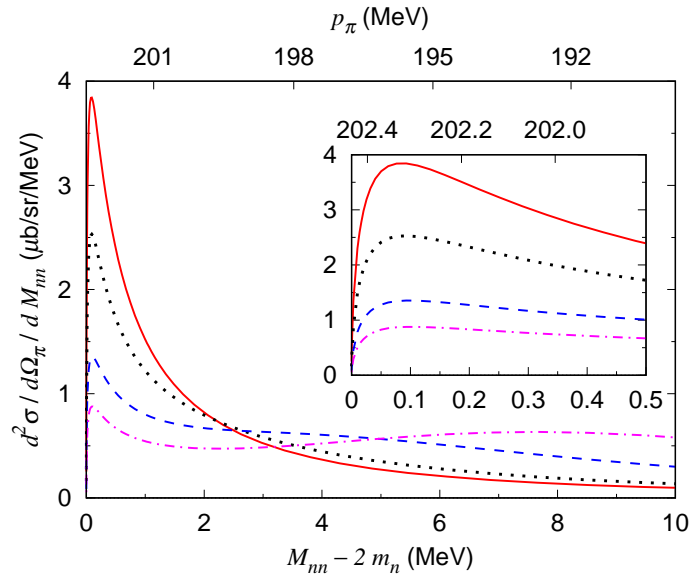


FIG. 6.  $M_{nn}$  distributions for  $\gamma d \rightarrow \pi^+ nn$  at different pion-emission angles ( $E_\gamma = 250$  MeV). The red solid, black dotted, blue dashed, and magenta dash-dotted curves are for  $\theta_\pi = 0^\circ$ ,  $15^\circ$ ,  $30^\circ$ , and  $45^\circ$ , respectively.

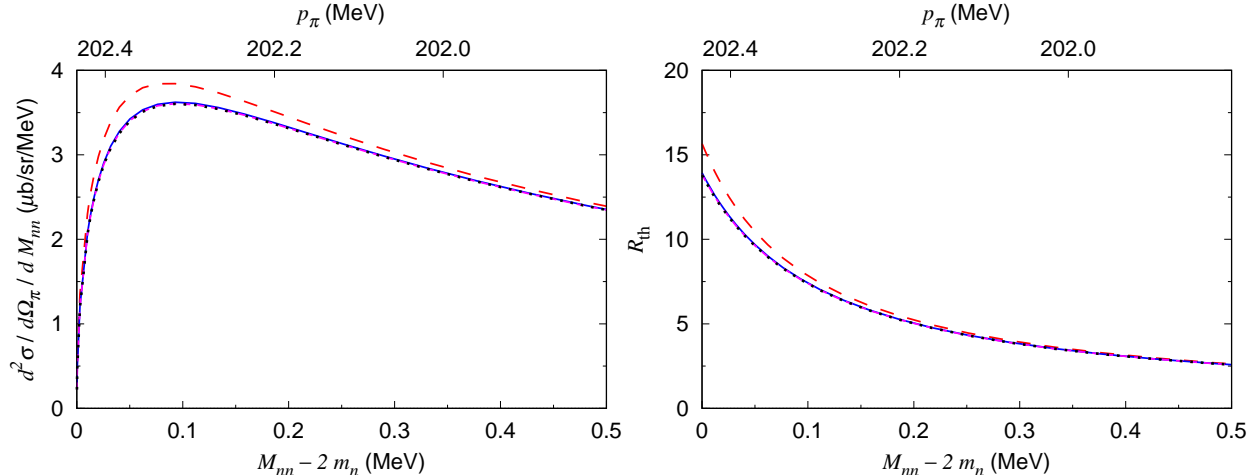


FIG. 7. (Left)  $M_{nn}$  distribution at  $E_\gamma = 250$  MeV calculated with different  $NN$  potentials. The red long-dashed, black dotted, blue solid, and magenta short-dashed curves are calculated with the CD-Bonn ( $a_{nn} = -18.9$  fm), Reid93 ( $a_{nn} = -17.3$  fm), and Nijmegen I ( $a_{nn} = -17.3$  fm), and Nijmegen II ( $a_{nn} = -17.3$  fm)  $NN$  potentials, respectively. The other conditions are the same as those in Fig. 3. (Right) Ratio  $R_{\text{th}}$  defined in Eq. (13) for the same condition as the left panel.

is also useful in extracting the photoproduction cross sections from an electron scattering experiment. Thus we use  $\theta_\pi = 0^\circ$  in the following calculation. As will be discussed later in Sec. IV, the choice of  $\theta_\pi = 0^\circ$  is also important to practically measure the  $\gamma d \rightarrow \pi^+ nn$  cross sections at the required precision and resolution.

We now examine various model dependences in  $d^2\sigma/d\Omega_\pi/dM_{nn}$  and  $R_{\text{th}}$  for  $\gamma d \rightarrow \pi^+ nn$ . As we will find later, the shape of  $R_{\text{th}}$  in  $M_{nn} - 2m_n < 0.5$  MeV ( $2 \text{ MeV} < M_{nn} - 2m_n < 6$  MeV) is useful to determine  $a_{nn}$  ( $r_{nn}$ ). Thus we pay a special attention to theoretical uncertainties on  $R_{\text{th}}$ , and quantify it as

$$\Delta R_{\text{th}}(M_{nn}) = \sqrt{\frac{1}{N_{\text{model}}} \sum_{i=1}^{N_{\text{model}}} [R_{\text{th}}^i(M_{nn}) - R_{\text{th}}(M_{nn})]^2}, \quad (16)$$

where  $R_{\text{th}}(M_{nn})$  is calculated with the standard setting that has been used in Figs. 3-6, while some dynamical contents have been replaced by a different model in  $R_{\text{th}}^i(M_{nn})$ .

We first examine the  $NN$  interaction model dependence. We use four high-precision phenomenological  $NN$  potentials to describe the  $NN$  rescattering and the deuteron wave function: the CD-Bonn potential [36], the Nijmegen I potential [37], the Nijmegen II potential [37], and the Reid93 potential [37], for which the scattering length is  $a_{nn} = -18.9, -17.3, -17.3,$  and  $-17.3$  fm, respectively, and the effective range is  $r_{nn} = 2.8$  fm for all. A comparison of  $d^2\sigma/d\Omega_\pi/dM_{nn}$  and  $R_{\text{th}}$  calculated with these different  $NN$  potentials is shown in Fig. 7. We can see that, around the peak region, the cross section with the CD-Bonn potential is  $\sim 10\%$  larger than the others because of the larger scattering length. On the other hand, the cross sections are essentially the same for the Nijmegen I, II, and Reid93 potentials for which  $a_{nn}$  and  $r_{nn}$  are the same. This result is not trivial because the  $NN$  amplitudes from these three  $NN$  models have rather different off-shell behaviors. Actually, in the previous work on  $\pi^- d \rightarrow \gamma nn$  [16], the authors found that the neutron

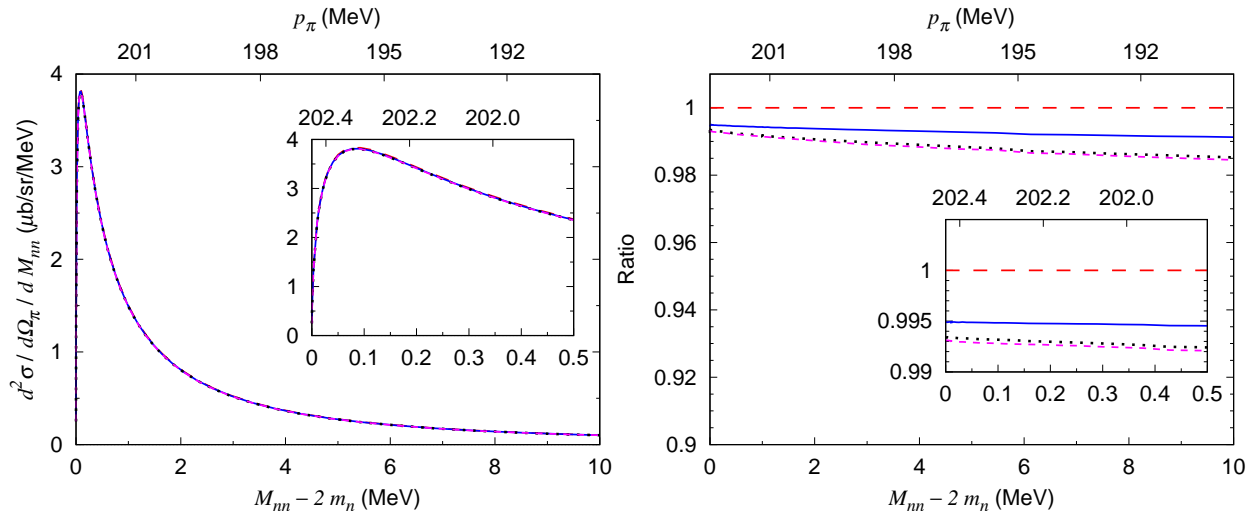


FIG. 8. (Left)  $M_{nn}$  distribution at  $E_\gamma = 250$  MeV calculated with the replacement in Eq. (17);  $a_{nn} = -18.9$  fm,  $r_{nn} = 2.75$  fm. The red long-dashed, black dotted, red solid, and magenta short-dashed curves are obtained with the CD-Bonn, Reid93, Nijmegen I, and Nijmegen II potentials, respectively. The four curves are almost the same. The other conditions are the same as those in Fig. 3. (Right) Ratios of the curves in the left panel. Each of the curves in the left panel is divided by the one from the CD-Bonn potential, and shown with the same feature.

time-of-flight spectrum obtained with the Nijmegen I potential is non-negligibly different from those with the Nijmegen II potential.

We further study effects from the off-shellness of the  $NN$  amplitude. As found in the previous works on  $\pi^- d \rightarrow \gamma nn$  [14, 16], the uncertainty of the off-shell behavior is the largest source of the model dependence of the extracted  $a_{nn}$ . We examine the  $NN$  model dependence of the off-shell effect. In order to see this clearly, we adjust the on-shell amplitudes from all different  $NN$  models be the same by using the following replacement in Eq. (6):

$$t_{NN}(M_{N_1 N_2}) \Rightarrow t_{NN,NN}^{\text{ERE}}(M_{N_1 N_2}) \times \left[ \frac{t_{NN}(M_{N_1 N_2})}{t_{NN,NN}^{\text{on-shell}}(M_{N_1 N_2})} \right], \quad (17)$$

where  $t_{NN,NN}^{\text{ERE}}$  is the  $NN$  amplitude parametrized with the effective range expansion of Eq. (1); we neglect  $O(p^4)$  contribution. The result obtained with this replacement is shown in Fig. 8(left). Within the considered high-precision  $NN$  potentials, the off-shell effect is very similar. In order to see the model dependence, we show in Fig. 8(right) ratios of the curves shown on the left panel. We also calculate the  $NN$  off-shell uncertainty of  $R_{\text{th}}$  using Eq. (16) with  $N_{\text{model}} = 3$  for the Nijmegen I, II, and Reid93 potentials. The calculated  $\Delta R_{\text{th}}$  is shown by the red solid curve in Fig. 9(left). The variation of the shape of  $R_{\text{th}}$  due to the uncertainty can be seen more clearly in  $\Delta R_{\text{th}}/R_{\text{th}}$  as shown in Fig. 9(right).

The uncertainty of the elementary  $\gamma p \rightarrow \pi^+ n$  amplitudes may affect the theoretically calculated  $M_{nn}$  distribution. This uncertainty would be examined by comparing calculations with different models for the amplitudes. We use the DCC model as before, and now also use the Chew-Mandelstam (CM12) parametrization [38] as another choice. The CM12 parametrization is a  $K$ -matrix fit to the  $\gamma N \rightarrow \pi N$  data and, by construction, it has only on-shell amplitudes. Thus, for comparison, we also use the on-shell DCC amplitudes. We show

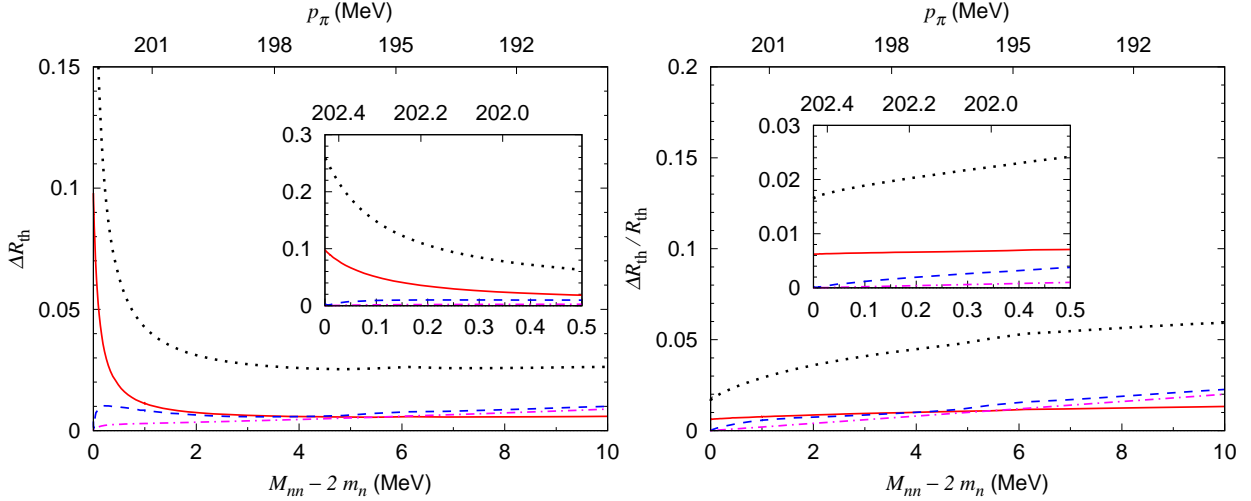


FIG. 9. Theoretical errors of  $R_{\text{th}}(M_{nn})$  defined in Eq. (16). (Left) The red solid, blue dashed, black dotted, and magenta dash-dotted curves are uncertainties of the  $NN$  potential, on-shell  $\gamma p \rightarrow \pi^+ n$  amplitudes, off-shell effects of  $\gamma p \rightarrow \pi^+ n$  amplitudes, and meson-exchange current effects, respectively. (Right) Each curve in the left panel is divided by  $R_{\text{th}}(M_{nn})$  with the standard setting.

in Fig. 10(left) the  $M_{nn}$  distributions of  $\gamma d \rightarrow \pi^+ nn$  at  $E_\gamma = 250$  MeV calculated with the DCC and CM12 elementary on-shell amplitudes. In this particular kinematics ( $\theta_\pi = 0^\circ$  and  $M_{nn} \sim 2m_n$ ), the cross sections obtained with the DCC model is slightly smaller than those with the CM12 solution. This reasonable agreement is due to the fact that both the DCC model and the CM12 parametrization well reproduce the  $\gamma p \rightarrow \pi^+ n$  data. Furthermore, the slight difference seen in Fig. 10(left) is almost perfectly removed in the ratio  $R_{\text{th}}$  as shown in Fig. 10(right). This shows that, by analyzing  $R_{\text{th}}$  and its experimental counterpart, we can study the low-energy  $nn$  scattering without being influenced by the uncertainty associated with the on-shell elementary  $\gamma p \rightarrow \pi^+ n$  amplitudes. The uncertainty of  $R_{\text{th}}$  due to the on-shell  $\gamma p \rightarrow \pi^+ n$  amplitudes is calculated using Eq. (16) with  $N_{\text{model}} = 1$  for the CM12, and shown in Fig. 9 by the blue dashed curve.

In the loop diagrams, the elementary  $\gamma p \rightarrow \pi^+ n$  amplitudes also bring about an uncertainty associated with their off-shell effects. Although the off-shell behavior of the DCC model has been constrained by fitting data to some extent, there would still exist some uncertainty. Thus we study the off-shell effect by using the on-shell elementary amplitudes in Eqs. (6) and (7), and comparing  $R_{\text{th}}$  from this calculation with the original one that considers the off-shell effect. The result is shown in Fig. 11. We can see that the off-shell effect reduces  $R_{\text{th}}$ , and thus the cross sections, by 1.7%–2.4% in  $M_{nn} - 2m_n \leq 0.5$  MeV and 4.0%–6.0% in  $2 \text{ MeV} < M_{nn} - 2m_n \leq 6$  MeV. Regarding the uncertainty of  $R_{\text{th}}$ , it is currently difficult to estimate because an off-shell  $\gamma p \rightarrow \pi^+ n$  amplitude from a different model is not available and thus we cannot study the model dependence. Thus we make a conservative estimate of the uncertainty due to the off-shell effects using Eq. (16) with  $N_{\text{model}} = 1$  for the calculation with the on-shell DCC  $\gamma p \rightarrow \pi^+ n$  amplitudes, and show the result in Fig. 9 by the black dotted curve.

Another source of theoretical uncertainty is contributions from meson-exchange currents,

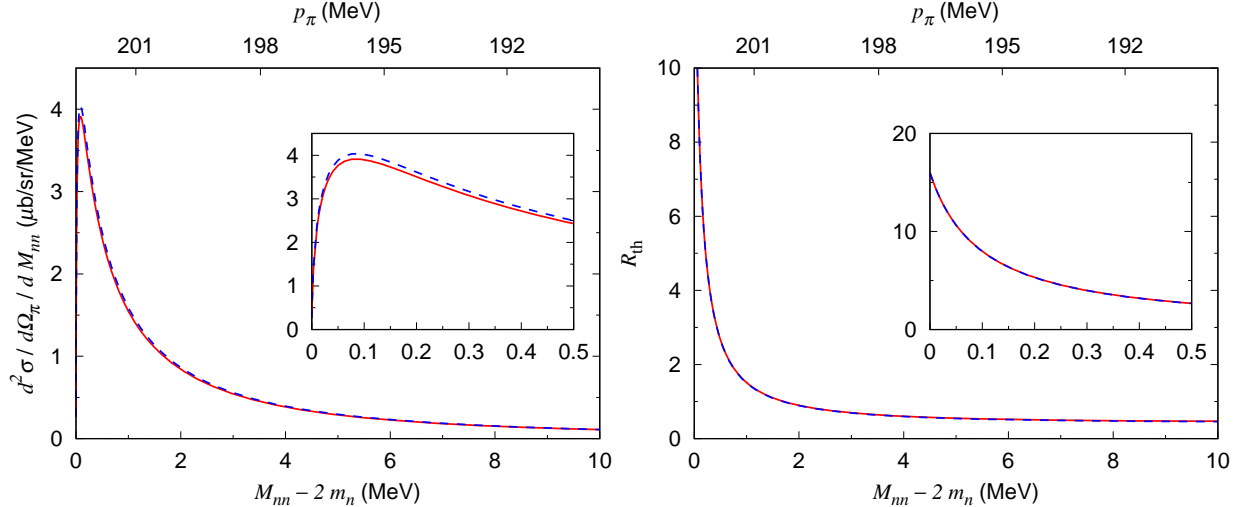


FIG. 10. (Left)  $M_{nn}$  distributions for different elementary amplitudes at  $E_\gamma = 250$  MeV. The red solid and blue dashed curves are obtained using on-shell  $\gamma p \rightarrow \pi^+ n$  amplitudes from the DCC model and the Chew-Mandelstam (CM12) parametrization [38], respectively. The other conditions are the same as those in Fig. 3. (Right) Ratio  $R_{\text{th}}$  defined in Eq. (13) for the same condition as the left panel.

other than those included in Fig. 2(c), not considered in the present model. The previous work on near-threshold  $\gamma d \rightarrow \pi^+ nn$  based on the chiral perturbation theory [17] also did not consider such mechanisms because they are higher-order effects within their counting scheme. Since we deal with the reaction at significantly higher photon energies, their argument does not necessarily apply to our case. A chiral perturbation theory calculation of  $\pi^- d \rightarrow nn\gamma$  [16] considered more meson-exchange currents. Still, they found that meson-exchange currents that can be accommodated by Fig. 2(c) give a leading effect. Therefore, we expect that meson-exchange current missing in our calculation gives a few % contribution to the cross sections, but the change in the shape would be even smaller. We thus assume that the missing meson-exchange current linearly increases  $R_{\text{th}}(M_{nn})$  of the standard setting as  $R_{\text{th}}^1(M_{nn}) = (1 + 0.002(M_{nn} - 2m_n)/\text{MeV}) \times R_{\text{th}}(M_{nn})$ . We then estimate the uncertainty  $\Delta R_{\text{th}}$  using Eq. (16) and show it in Fig. 9 by the magenta dash-dotted curve.

We now study the dependence of  $d^2\sigma/d\Omega_\pi/dM_{nn}$  and  $R_{\text{th}}$  on the scattering parameters  $a_{nn}$  and  $r_{nn}$ . For this purpose, we again use Eq. (17) to calculate the  $NN$  rescattering amplitudes. As we have seen above, various model-dependence change the absolute magnitude of  $d^2\sigma/d\Omega_\pi/dM_{nn}$  and  $R_{\text{th}}$  by a few percents level, while their shapes are rather stable. In order to extract  $a_{nn}$  and  $r_{nn}$  at the precision of  $\lesssim 0.5$  fm, which is comparable to the previous determinations [9–12], we thus use only the shape of ( $d^2\sigma/d\Omega_\pi/dM_{nn}$  and )  $R_{\text{th}}$  to determine the scattering parameters. First we vary  $a_{nn}$  from  $-16$  fm to  $-20$  fm, with  $r_{nn} = 2.75$  fm fixed, and show the obtained  $d^2\sigma/d\Omega_\pi/dM_{nn}$  and  $R_{\text{th}}$  in Fig. 12. The effect of changing  $a_{nn}$  is seen only in a small region of  $M_{nn} - 2m_n \lesssim 0.3$  MeV. When  $a_{nn}$  is changed by 1 fm, the cross section changes at most by  $\sim 10\%$  at  $M_{nn} \sim 2m_n$ , and by 4%–5% ( $\sim 0.17$   $\mu\text{b}/\text{sr}/\text{MeV}$ ) at  $M_{nn} - 2m_n = 0.07$ – $0.10$  MeV where the cross section reaches its peak. Because the shape of  $d^2\sigma/d\Omega_\pi/dM_{nn}$  and thus  $R_{\text{th}}$  sensitively changes as  $a_{nn}$  changes, fitting  $R_{\text{th}}$  to the corresponding data over  $M_{nn} - 2m_n \lesssim 0.3$  MeV would be an efficient way

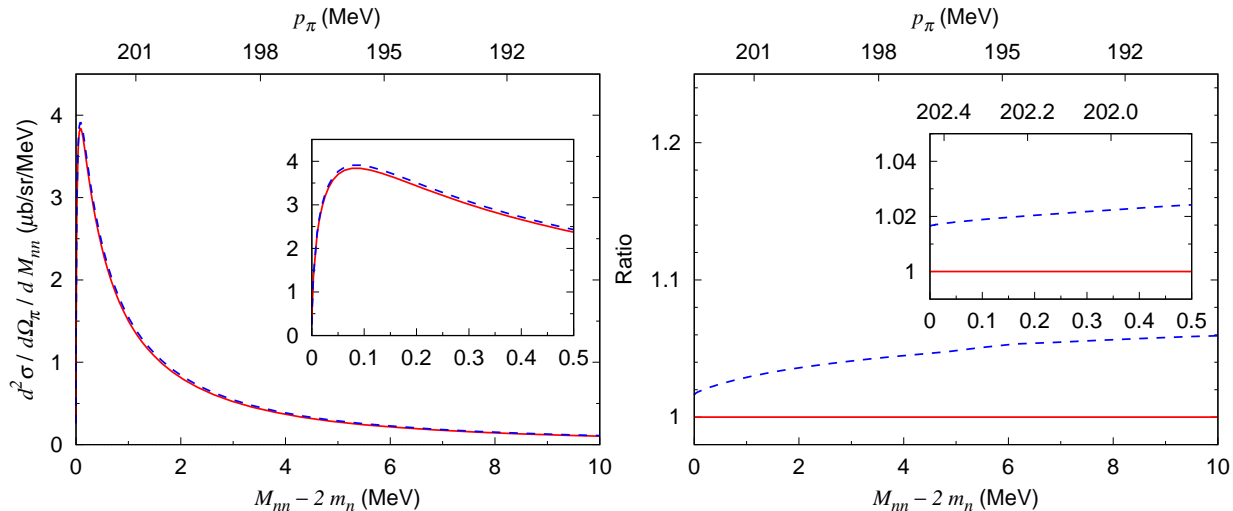


FIG. 11. (Left)  $M_{nn}$  distributions at  $E_\gamma = 250$  MeV with and without off-shell effects from  $\gamma p \rightarrow \pi^+ n$  amplitudes. The red solid curve represents the original calculation, and the blue dashed curve is obtained by replacing the off-shell amplitudes with the on-shell ones. (Right) Ratios of the curves in the left panel. Each of the curves is divided by the red curve in the left panel, and shown with the same feature.

to precisely determine  $a_{nn}$ .

Next we study the  $r_{nn}$  dependence. This time, we vary  $r_{nn}$  from 1 fm to 4 fm, with fixed  $a_{nn} = -18.9$  fm. The result is given for  $M_{nn} - 2m_n < 0.5$  MeV in Fig. 13 and for  $1 \text{ MeV} < M_{nn} - 2m_n < 10$  MeV in Fig. 14. For the negative  $a_{nn}$ , the  $NN$  rescattering amplitude of Fig. 2(b) becomes weaker as the positive  $r_{nn}$  increases. Thus, as  $r_{nn}$  increases, the cross section reduces (increases) in the small (large)  $M_{nn}$  region where the  $NN$  rescattering (impulse) amplitude dominates. When  $r_{nn}$  is increased by 1 fm, at  $M_{nn} - 2m_n \sim 0.1$  MeV, the cross section is reduced by  $\sim 1.5\%$  ( $\sim 0.06 \mu\text{b/sr/MeV}$ ). As discussed in the above paragraph, the shape of  $R_{\text{th}}$  is sensitive to  $a_{nn}$  in  $M_{nn} - 2m_n \lesssim 0.3$  MeV. In this  $M_{nn}$  region, the shape of  $R_{\text{th}}$  also depends on  $r_{nn}$  as seen in the inlet of Fig. 13. If  $r_{nn}$  is in the range of  $|r_{nn} - 2.75 \text{ fm}| < 0.5$  fm, as expected from Eq. (2), the shape of  $R_{\text{th}}$  changes from those for  $r_{nn} = 2.75$  fm by less than 1%. Thus it is important to control  $r_{nn}$  at the 0.5 fm level. Although old data have been used to constrain  $r_{nn}$  (see Ref. [39] for review), it would be desirable to use the  $\gamma d \rightarrow \pi^+ nn$  data to directly constrain  $r_{nn}$ , at the precision of 0.5 fm, without resorting to the charge symmetry. As found in the inlet of Fig. 14(right), the shape of  $R_{\text{th}}$  for  $2 \text{ MeV} < M_{nn} - 2m_n < 6$  MeV shows a good sensitivity to  $r_{nn}$  while no sensitivity to  $a_{nn}$ .

We now perform a Monte Carlo simulation and estimate uncertainties of  $a_{nn}$  and  $r_{nn}$  extracted from  $R_{\text{exp}}$ , an experimental counterpart to  $R_{\text{th}}$ , under some realistic settings such as different finite  $M_{nn}$  bin widths and different precisions of  $R_{\text{exp}}$ . The  $R_{\text{exp}}$  data are generated with the fixed values of  $a_{nn}^\circ$  and  $r_{nn}^\circ$ . Specifically, we go through a procedure defined by the following four steps:

- (i) We introduce  $R_{\text{exp}}^\circ(a_{nn}^\circ, r_{nn}^\circ; M_{nn}) \equiv R_{\text{th}}(a_{nn}^\circ, r_{nn}^\circ; M_{nn}) + g \Delta R_{\text{th}}^{\text{all}}(M_{nn})$  where  $\Delta R_{\text{th}}^{\text{all}}(M_{nn})$  is the quadratic sum of  $\Delta R_{\text{th}}(M_{nn})$ s from different sources shown in Fig. 9(left). The parameter  $g$  is randomly generated at every cycle according to the standard normal

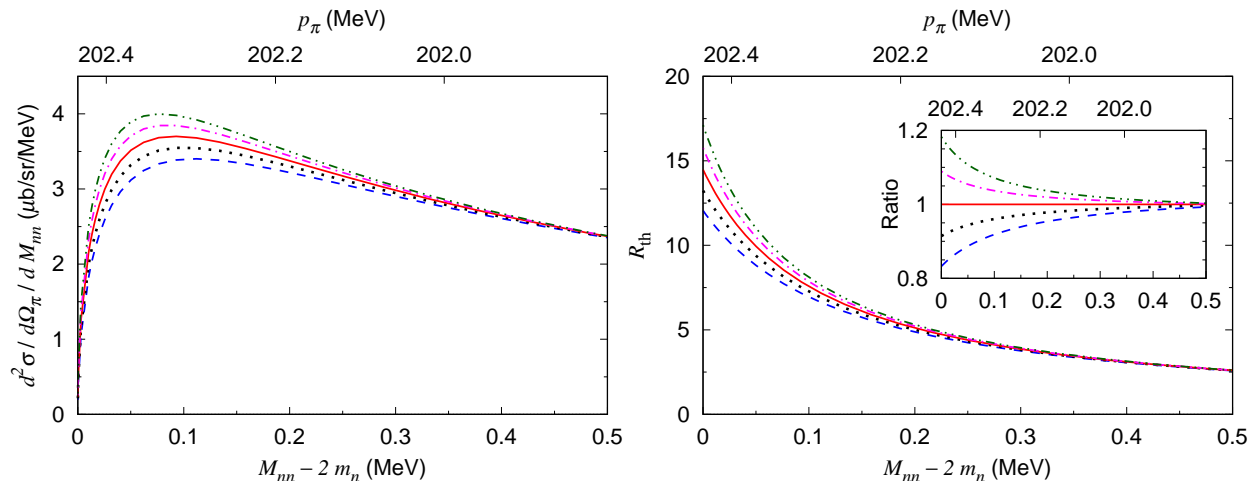


FIG. 12.  $M_{nn}$  distributions for different scattering length ( $a_{nn}$ ) values. The blue dashed, black dotted, red solid, magenta dash-dotted, and green dash-two-dotted curves are calculated with  $a_{nn} = -16, -17, -18, -19,$  and  $-20$  fm, respectively;  $r_{nn} = 2.75$  fm. The off-shell dependence of the  $NN$  amplitudes are taken from the CD-Bonn potential as explained in the text. In the inset, each of  $R_{th}$  is divided by  $R_{th}$  of  $a_{nn} = -18$  fm. The other conditions are the same as those in Fig. 3.

distribution.

- (ii) The histogram  $R_{exp}^{\circ}(a_{nn}^{\circ}, r_{nn}^{\circ}; i)$  for the  $i$ -th bin is given by averaging  $R_{exp}^{\circ}(a_{nn}^{\circ}, r_{nn}^{\circ}; M_{nn})$  with respect to  $M_{nn}$  over the bin width.
- (iii) The histogram data  $R_{exp}(i)$  is generated from  $R_{exp}^{\circ}(i)$  by including a statistical fluctuation corresponding to the given precision.
- (iv) We simultaneously search for  $a_{nn}$  and  $r_{nn}$  with which  $R_{exp}(a_{nn}, r_{nn}; M_{nn})$ , averaged over the bin width, optimally fits  $R_{exp}(i)$  in the  $M_{nn}$  range of  $[0.00, 6.00]$  MeV. We are allowed to multiply a free overall coefficient to  $R_{exp}(a_{nn}, r_{nn}; M_{nn})$  since we just try to reproduce the shape.

The above procedure is repeated many (10,000) times, and the width of the obtained  $a_{nn}$  ( $r_{nn}$ ) distribution corresponds to the uncertainty. This analysis is done at several different values of  $a_{nn}^{\circ}$  and  $r_{nn}^{\circ}$  over  $-20 \text{ fm} \leq a_{nn}^{\circ} \leq -15 \text{ fm}$  and  $1 \text{ fm} \leq r_{nn}^{\circ} \leq 5 \text{ fm}$ . The centroid values of  $a_{nn}$  and  $r_{nn}$  reproduce  $a_{nn}^{\circ}$  and  $r_{nn}^{\circ}$  very well. The  $a_{nn}$  uncertainty is approximately proportional to the  $R_{exp}$  precision. When the  $M_{nn}$  bin width is taken to be 0.04 MeV, the precision of 5% is required to make the  $a_{nn}$  uncertainty less than 0.5 fm. With the same bin width, the  $r_{nn}$  uncertainty is  $\lesssim 0.1$  fm ( $\sim 0.05$  fm) for the precision of 5% (0%). A smaller bin width results in a smaller  $a_{nn}$  uncertainty ( $\Delta a_{nn} = 0.13$ – $0.27$  fm for the bin width of 0.01–0.08 MeV) but a larger  $r_{nn}$  uncertainty ( $\Delta r_{nn} = 0.23$ – $0.06$  fm for the bin width of 0.01–0.08 MeV) owing to the theoretical uncertainties  $\Delta R_{th}$ s. The above results do not change very much within the specified range of  $a_{nn}^{\circ}$ . When we take  $a_{nn}^{\circ} = -18.9$  fm and  $r_{nn}^{\circ} = 2.75$  fm, the uncertainties of the  $a_{nn}$  and  $r_{nn}$  values are found to be 0.21 and 0.06 fm, respectively, for 0.04 MeV bin width and  $\pm 2\%$  precision of  $R_{exp}$  in each bin.

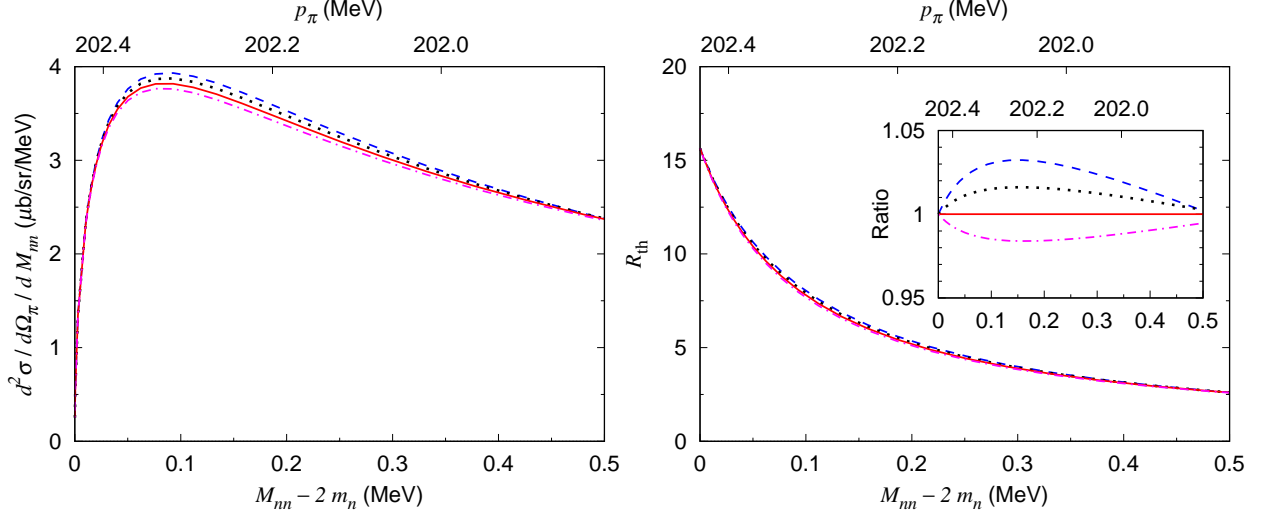


FIG. 13.  $M_{nn}$  distributions for different effective range ( $r_{nn}$ ) values. The blue dashed, black dotted, red solid, and magenta dash-dotted curves are calculated with  $r_{nn} = 1, 2, 3,$  and  $4$  fm, respectively;  $a_{nn} = -18.9$  fm. In the inset, each of  $R_{\text{th}}$  is divided by  $R_{\text{th}}$  of  $r_{nn} = 3$  fm. The other conditions are the same as those in Fig. 12.

#### IV. EXPERIMENTAL STRATEGY TO EXTRACT HIGH-RESOLUTION $\gamma d \rightarrow \pi^+ nn$ DATA FROM PION ELECTROPRODUCTION DATA

In this section, we discuss how to experimentally obtain high resolution  $M_{nn}$  distribution data of  $\gamma d \rightarrow \pi^+ nn$  to be used for determining the  $nn$  scattering parameters. Since we do not detect neutrons, the momenta and angles of the photon and pion must be measured with sufficiently high resolutions. Considering the currently available experimental facilities in the world, we cannot achieve such high resolutions with a real photon beam. However, we can

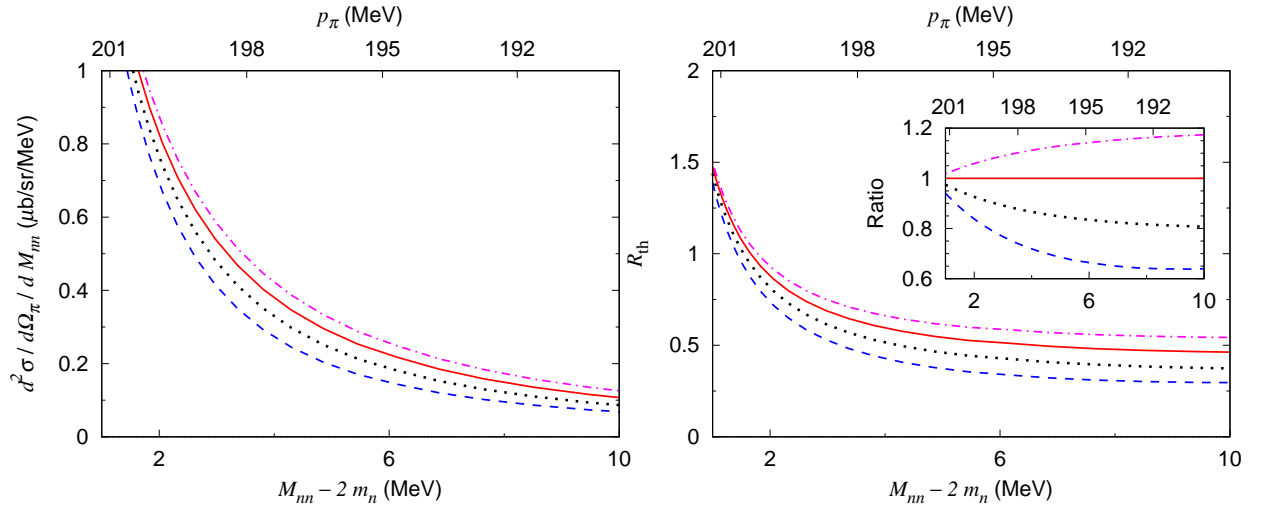


FIG. 14. Same as Fig. 13 but for  $1 \text{ MeV} \leq M_{nn} - 2m_n \leq 10 \text{ MeV}$ .

achieve such a high  $M_{nn}$  resolution utilizing virtual photons ( $\gamma^*$ )s from electron scattering and two magnetic spectrometers to detect the scattered electrons and the emitted positive pions. Tuning the electron scattering kinematics, we can measure cross sections for pion production with a so-called almost-real photon at low momentum transfer ( $Q^2 \sim 0$ ).

The triple-differential unpolarized cross section for the  $(e, e'\pi)$  reaction can be written in the following form (differentiation with respect to  $M_{nn}$  being omitted):

$$\frac{d^3\sigma}{dE_{e'} d\Omega_{e'} d\Omega_\pi} = \Gamma_\gamma \left\{ \frac{d\sigma_T}{d\Omega_\pi} + \epsilon_L \frac{d\sigma_L}{d\Omega_\pi} + \sqrt{2\epsilon_L(1+\epsilon_T)} \frac{d\sigma_{LT}}{d\Omega_\pi} + \epsilon_T \frac{d\sigma_{TT}}{d\Omega_\pi} \cos 2\phi_\pi \right\}, \quad (18)$$

where the electron mass has been neglected, and  $\sigma_T$ ,  $\sigma_L$ ,  $\sigma_{LT}$ , and  $\sigma_{TT}$  are the transverse, longitudinal, longitudinal-transverse interference, and transverse-transverse interference cross sections, respectively [40]. We introduce

$$\epsilon_T = \left( 1 + \frac{2|\mathbf{q}|^2}{Q^2} \tan^2 \frac{\theta_{e'}}{2} \right)^{-1} \quad \text{and} \quad \epsilon_L = \frac{Q^2}{\omega^2} \epsilon_T, \quad (19)$$

with  $\theta_{e'}$  the electron scattering angle in the laboratory frame and  $Q^2 = -(\omega^2 - |\mathbf{q}|^2)$  the squared momentum transfer;  $(\omega, \mathbf{q})$  is the four-momentum transfer from the electron to the deuteron. The pion angle  $\Omega_\pi = (\theta_\pi, \phi_\pi)$  is measured with respect to the virtual photon direction, and  $\phi_\pi$  is the angle between the electron-scattering  $(e, e')$  plane and the pion-production  $(\gamma^*, \pi)$  plane. The factor  $\Gamma_\gamma$  in Eq. (18) denotes the virtual photon flux given by

$$\Gamma_\gamma = \frac{\alpha}{2\pi^2 Q^2} \frac{E_\gamma}{1 - \epsilon_T} \frac{E_{e'}}{E_e}, \quad (20)$$

with  $E_e$  ( $E_{e'}$ ) the incident (scattered) electron energy,  $\alpha$  the fine structure constant, and  $E_\gamma = \omega - Q^2/2m_d$  the corresponding real photon energy in the laboratory frame. The virtual photon emission angle  $\theta_\gamma$  is specified by  $\cos \theta_\gamma = (\mathbf{p}_e \cdot \mathbf{q}) / (|\mathbf{p}_e||\mathbf{q}|)$ . In Eq. (18), all the cross sections depend on  $E_\gamma$  and  $Q^2$ .

Elementary  $\gamma N \rightarrow \pi N$  data [ $d\sigma_T/d\Omega_\pi(Q^2 = 0)$ ] are generally more precisely measured than  $\gamma^* N \rightarrow \pi N$  data [ $d\sigma_T/d\Omega_\pi(Q^2 \neq 0)$ ] from pion electroproductions. A main reason is that an uncertainty enters into the data when separating  $d\sigma_T/d\Omega_\pi$  from  $d\sigma_L/d\Omega_\pi$ ,  $d\sigma_{LT}/d\Omega_\pi$ , and  $d\sigma_{TT}/d\Omega_\pi$  for  $\gamma^* N \rightarrow \pi N$ . As a consequence, the  $Q^2 = 0$  sector of the DCC model as well as other similar models for  $\gamma^{(*)} N \rightarrow \pi N$  is significantly better tested by the real photon data, in comparison with the finite  $Q^2$  sector of the models. Therefore, for a reliable determination of the  $nn$  scattering parameters using such models, almost-real photon data of  $\gamma d \rightarrow \pi^+ nn$ ,  $d\sigma_T/d\Omega_\pi$  in Eq. (18) at  $Q^2 \sim 0$ , are highly preferred.

Let us consider a method to extract  $d\sigma_T/d\Omega_\pi$  at  $Q^2 \sim 0$  from the  $d(e, e'\pi^+)nn$  cross sections. The  $d\sigma_{LT}/d\Omega_\pi$  and  $d\sigma_{TT}/d\Omega_\pi$  terms in Eq. (18) vanish at  $\theta_\pi = 0$  because they are proportional to  $\sin \theta_\pi$  and  $\sin^2 \theta_\pi$ , respectively. Fortunately,  $\gamma d \rightarrow \pi^+ nn$  data at  $\theta_\pi = 0$  is exactly what we need, as we have discussed in connection with Fig. 6. Now Eq. (18) at  $\theta_\pi = 0$  becomes a simpler form:

$$\frac{d^3\sigma}{dE_{e'} d\Omega_{e'} d\Omega_\pi} = \Gamma_\gamma \left\{ \frac{d\sigma_T}{d\Omega_\pi} + \epsilon_L \frac{d\sigma_L}{d\Omega_\pi} \right\}. \quad (21)$$

The  $\epsilon_L d\sigma_L/d\Omega_\pi$  contribution can be made smaller by taking a kinematics where  $\epsilon_L$  and  $Q^2$  are low. Even when the  $\epsilon_L d\sigma_L/d\Omega_\pi$  contribution cannot be made negligibly small, we can still separate out  $d\sigma_T/d\Omega_\pi$  utilizing the linear  $\epsilon_L$  dependence in Eq. (21).

TABLE I. Summary of the parameters for the three spectrometers at Mainz MAMI. The parameters are taken from Ref. [41].

spectrometer	SpekA	SpekB	SpekC
minimum angle	18°	7°	18°
maximum angle	160°	62°	160°
horizontal angular coverage (mrad)	±100	±20	±100
vertical angular coverage (mrad)	±70	±70	±70
angular resolution at the target position (mrad)	< 3	< 3	< 3
momentum bite	±20%	±15%	±25%
momentum resolution ( $\delta p/p$ )	$10^{-4}$	$10^{-4}$	$10^{-4}$

The A1 spectrometer facility at Mainz MAMI [41] is an outstanding candidate to conduct an experiment under the above-discussed kinematical and precision conditions. The facility is capable of providing the high energy-resolution electron beams ( $\delta p/p < 10^{-4}$ ) and measuring the momenta and angles of electrons and pions with high resolutions,  $\delta p/p = 10^{-4}$  and  $\delta\theta < 3$  mrad ( $0.2^\circ$ ), required to determine the  $nn$  scattering parameters. Three magnetic spectrometers called SpekA, SpekB, and SpekC are placed in a horizontal plane ( $\phi_\pi = 0^\circ$ ). SpekA and SpekC, each of which covers  $\pm 100$  mrad ( $\pm 5.7^\circ$ ), can be placed between  $18^\circ$  to  $160^\circ$  from the primary electron beam direction. SpekB can be placed at more forward angles from  $7^\circ$  to  $62^\circ$ , and it has a relatively smaller coverage of  $\pm 20$  mrad ( $\pm 1.1^\circ$ ). Table I lists a brief summary of the parameters for the three spectrometers at Mainz MAMI.

The experimental constraints do not allow us to take a kinematical setting where  $\epsilon_L d\sigma_L/d\Omega_\pi$  is negligibly small compared to  $d\sigma_T/d\Omega_\pi$ . Thus a realistic solution is to separate the  $d\sigma_T/d\Omega_\pi$  and  $d\sigma_L/d\Omega_\pi$  contributions by taking advantage of the linear  $\epsilon_L$  dependence in Eq. (21). For this purpose, we need to measure cross sections at several kinematical points where  $\omega$  and  $Q^2$ , and thus  $d\sigma_T/d\Omega_\pi$  and  $d\sigma_L/d\Omega_\pi$ , are the same, while  $\epsilon_L$  is different. In addition,  $Q^2$  must be small enough to regard the virtual photon as real. Suppose we utilize SpekA (or SpekC) and SpekB for detecting the scattered electron and emitted positive pion, respectively. To obtain  $E_\gamma = 200$  (250) MeV under the constraints of  $\theta_{e'} \geq 12.3^\circ$  and  $\theta_\gamma \geq 5.9^\circ$ , the minimum  $Q^2$  achievable is 0.0021 (0.0013)  $\text{GeV}^2/c^2$  and  $\epsilon_L = 1.92\%$ . At this  $Q^2$  value, the experimental constraints do not allow us to change  $\epsilon_L$  and thus the  $\sigma_T$ - $\sigma_L$  separation is impossible. In order to cover a wide range of  $\epsilon_L$  for the separation, we choose  $Q^2 = 0.0050 \text{ GeV}^2/c^2$ . For using the virtual photon of  $Q^2 = 0.0050 \text{ GeV}^2/c^2$  and  $E_\gamma = 200$  or 250 MeV, relations between kinematical variables of electron and photon ( $E_e$ ,  $E_{e'}$ ,  $\theta_{e'}$ ,  $\epsilon_L$ , and  $\theta_\gamma$ ) are given as shown in Fig. 15. The experimental constraint ( $\theta_\gamma \geq 5.9^\circ$ ) requires  $E_e \geq 230$  (300) MeV for  $E_\gamma = 200$  (250) MeV, giving  $\epsilon_L \geq 2.24\%$  (2.17%). The  $d(e, e'\pi^+)nn$  cross sections measured at several electron kinematics in Fig. 15 can be used for the  $\sigma_T$ - $\sigma_L$  separation, providing  $d\sigma_T/d\Omega_\pi$  at  $Q^2 = 0.0050 \text{ GeV}^2/c^2$ .

We note that, within the  $\gamma d \rightarrow \pi^+ nn$  model used in this work,  $d\sigma_T/d\Omega_\pi$  at  $Q^2 = 0$  is slightly larger by  $\sim 1\%$  than those at  $Q^2 = 0.0050 \text{ GeV}^2/c^2$ , and the shape of the  $M_{nn}$  distribution hardly changes. Therefore, we can directly apply the analysis method and results for the real photon, presented in the previous sections, to the data of  $d\sigma_T/d\Omega_\pi$  at  $Q^2 = 0.0050 \text{ GeV}^2/c^2$  for determining the  $nn$  scattering parameters. Also, thanks to the high angle resolution ( $< 3$  mrad) of the facility, we do not need to modify the presented

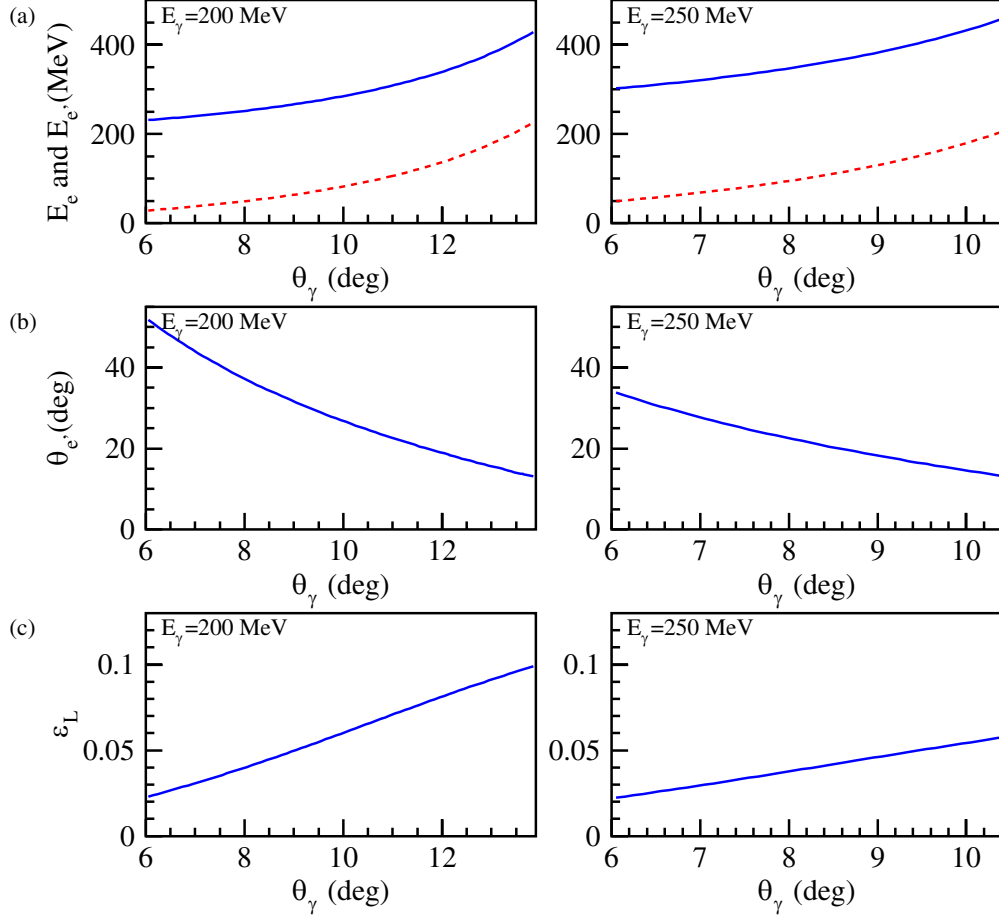


FIG. 15. (a) Incident electron energy  $E_e$  (blue solid) and scattered electron energy  $E_{e'}$  (red dashed) as a function of the emission angle of virtual photons in the laboratory frame  $\theta_\gamma$  at  $Q^2 = 0.0050$   $\text{GeV}^2/c^2$  for  $E_\gamma = 200$  MeV (left) and 250 MeV (right). (b) electron scattering angle  $\theta_{e'}$ . (c) degree of longitudinal polarization  $\epsilon_L$ .

results for the finite angle resolution.

## V. SUMMARY

We have discussed the possibility of extracting the low-energy neutron-neutron scattering parameters  $a_{nn}$  and  $r_{nn}$  from  $\gamma d \rightarrow \pi^+ nn$  cross section data. The analysis is based on a theoretical model for  $\gamma d \rightarrow \pi^+ nn$  that incorporates realistic elementary amplitudes for  $\gamma p \rightarrow \pi^+ n$ ,  $NN \rightarrow NN$ , and  $\pi N \rightarrow \pi N$ . We showed that  $\gamma d \rightarrow \pi^+ nn$  at the special kinematics with  $\theta_\pi = 0^\circ$  and  $E_\gamma \sim 250$  MeV would be suitable to study the neutron-neutron scattering in the low  $nn$  invariant mass region ( $M_{nn} \sim 2m_n$ ). This is because the  $NN$  rescattering mechanism dominates while the  $\pi N \rightarrow \pi N$  rescattering contribution is negligibly small. We assessed theoretical uncertainties from various sources such as on- and off-shell behaviors of the  $\gamma p \rightarrow \pi^+ n$  and  $NN \rightarrow NN$  amplitudes. This assessment shows that the shape of the ratio  $R_{\text{th}}$ , defined with  $\gamma d \rightarrow \pi^+ nn$  cross section ( $d^2\sigma/dM_{nn}/d\Omega_\pi$ ) as in Eq. (13), is particularly useful for extracting  $a_{nn}$  and  $r_{nn}$  from data because it has a

good sensitivity to these scattering parameters and significantly reduced model dependences compared to  $d^2\sigma/dM_{nn}/d\Omega_\pi$ . The experimental counterpart to  $R_{\text{th}}$ ,  $R_{\text{exp}}$ , is given with measurable  $\gamma d \rightarrow \pi^+ nn$  and  $\gamma p \rightarrow \pi^+ n$  cross sections and the deuteron wave function. We have found that  $R_{\text{exp}}$  with 2% error, resolved into the  $M_{nn}$  bin width of 0.04 MeV, can determine  $a_{nn}$  and  $r_{nn}$  with uncertainties of  $\pm 0.21$  fm and  $\pm 0.06$  fm, respectively, for the case of  $a_{nn} = -18.9$  fm and  $r_{nn} = 2.75$  fm; the uncertainties do not change significantly when the  $a_{nn}$  value is changed from  $-20$  to  $-15$  fm. Such a high  $M_{nn}$  resolution can be achieved with an electron scattering experiment that utilizes the A1 spectrometer facility at Mainz MAMI. The  $d^2\sigma/dM_{nn}/d\Omega_\pi$  for  $d(\gamma, \pi^+)nn$  can be separated from  $d^4\sigma/dE_{e'}/d\Omega_{e'}/dM_{nn}/d\Omega_\pi$  for  $d(e, e'\pi^+)nn$  at different  $\epsilon_L$  values but at the same  $Q^2 \simeq 0$  (the almost-real photon condition). Since the proposed method does not require a difficult experimental task of dealing with the neutron detection efficiency and its uncertainty, the method has a great advantage in this regard over the previous one that extracts  $a_{nn}$  from the neutron time-of-flight spectrum of  $\pi^- d \rightarrow \gamma nn$ .

## ACKNOWLEDGMENTS

This work was supported in part by the Japan Society for the Promotion of Science (JSPS) through Grants-in-Aid for Scientific Research (B) No. 19H01902, and for Scientific Research on Innovative Areas Nos. 19H05104, 19H05141 and 19H05181, and also by National Natural Science Foundation of China (NSFC) under contracts 11625523.

- 
- [1] G.A. Miller, B.M.K. Nefkens, and I. Slaus, Phys. Rept. **194**, 1 (1990).
  - [2] G.A. Miller and W.T.H. van Oers, *Symmetries and fundamental interactions in nuclei*, eds. W.C. Haxton, and E.M. Henley, p. 127 (1994), arXiv:nucl-th/9409013.
  - [3] R. Abegg *et al.*, Phys. Rev. Lett. **56**, 2571 (1986); Phys. Rev. D **39**, 2464 (1989).
  - [4] A.K. Opper *et al.*, Phys. Rev. Lett. **91**, 212302 (2003).
  - [5] T.O. Yamamoto *et al.* (J-PARC E13 Collaboration), Phys. Rev. Lett. **115**, 222501 (2015).
  - [6] A. Esser *et al.* (A1 Collaboration), Phys. Rev. Lett. **114**, 232501 (2015).
  - [7] A. Gårdestig, J. Phys. G **36**, 053001 (2009).
  - [8] H. Witała, W. Glöckle, and Th. Cornelius, Phys. Rev. C **39**, 384 (1989); W. Glöckle, H. Witała, D. Hüber, H. Kamada, and J. Golak, Phys. Rep. **274**, 107 (1996).
  - [9] V. Huhn *et al.*, Phys. Rev. Lett. **85**, 1190 (2000).
  - [10] D.E. Gonzalez Trotter *et al.*, Phys. Rev. C **73**, 034001 (2006).
  - [11] W. von Witsch *et al.*, Phys. Rev. C **74**, 014001 (2006).
  - [12] Q. Chen *et al.*, Phys. Rev. C **77**, 054002 (2008).
  - [13] C.R. Howell *et al.*, Phys. Lett. B **444**, 252 (1998).
  - [14] W.R. Gibbs, B.F. Gibson, and G.J.Jr Stephenson, Phys. Rev. C **11**, 90 (1975); *ibid.* **12**, 2130 (1975); *ibid.* **16**, 322 (1977); *ibid.* **16**, 327 (1977).
  - [15] G.F. de Téra mond, Phys. Rev. C **16**, 1976 (1977); G.F. de Téra mond, J. Páez, and C.W. Soto Vargas, Phys. Rev. C **21**, 2542 (1980); G.F. de Téra mond, and B. Gabioud, Phys. Rev. C **36**, 69 (1987).
  - [16] A. Gårdestig and D.R. Phillips, Phys. Rev. C **73**, 014002 (2006); Phys. Rev. Lett. **96**, 232301 (2006); A. Gårdestig, Phys. Rev. C **74**, 017001 (2006).

- [17] V. Lensky *et al.*, Eur. Phys. J. A **33**, 339 (2007).
- [18] H. Kamano, S.X. Nakamura, T.-S.H. Lee, and T. Sato, Phys. Rev. C **88**, 035209 (2013).
- [19] H. Kamano, S.X. Nakamura, T.-S.H. Lee, and T. Sato, Phys. Rev. C **94**, 015201 (2016).
- [20] S.X. Nakamura, H. Kamano, and T. Sato, Phys. Rev. D **92**, 074024 (2015).
- [21] S.X. Nakamura *et al.*, Rep. Prog. Phys. **80**, 056301 (2017).
- [22] J.E. Sobczyk, E. Hernández, S.X. Nakamura, J. Nieves, and T. Sato, Phys. Rev. D **98**, 073001 (2018).
- [23] J. Ahrens *et al.* (GDH and A2 Collaborations), Eur. Phys. J. A **21**, 323 (2004).
- [24] A.K. Kerman, H. McManus, and R.M. Thaler, Ann. Phys. **8**, 551 (1959).
- [25] E.M. Darwish, H. Arenhövel and M. Schwamb, Eur. Phys. J. **A16**, 111 (2003).
- [26] A. Fix and H. Arenhövel, Phys. Rev. C **72**, 064005 (2005).
- [27] M.I. Levchuk, A.Yu. Loginov, A.A. Sidorov, V.N. Stibunov, and M. Schumacher, Phys. Rev. C **74**, 014004 (2006).
- [28] M. Schwamb, Phys. Rep. **485**, 109 (2010).
- [29] J.-J. Wu, T. Sato, and T.-S.H. Lee, Phys. Rev. C **91**, 035203 (2015).
- [30] V.E. Tarasov, W.J. Briscoe, M. Dieterle, B. Krusche, A.E. Kudryavtsev, M. Ostrick, and I.I. Strakovsky, Phys. Atom. Nucl. **79**, 216 (2016).
- [31] S.X. Nakamura, H. Kamano, T.-S.H. Lee, and T. Sato, arXiv:1804.04757.
- [32] S.X. Nakamura, H. Kamano, and T. Ishikawa, Phys. Rev. C **96**, 042201 (2017).
- [33] S.X. Nakamura, Phys. Rev. C **98**, 042201 (2018).
- [34] S.X. Nakamura, H. Kamano, and T. Sato, Phys. Rev. D **99**, 031301 (2019).
- [35] L. Alvarez-Ruso *et al.*, Prog. Part. Nucl. Phys. **100**, 1 (2018).
- [36] R. Machleidt, Phys. Rev. C **63**, 024001 (2001).
- [37] V.G.J. Stoks, R.A.M. Klomp, C.P.F. Terheggen, and J.J. de Swart, Phys. Rev. C **49**, 2950 (1994).
- [38] R.L. Workman, M.W. Paris, W.J. Briscoe, I.I. Strakovsky Phys. Rev. C **86**, 015202 (2012).
- [39] I. Šlaus, Y. Akaishi, and H. Tanaka, Phys. Rep. **173**, 257 (1989); and references therein.
- [40] D. Dreschsel, and L. Tiator, J. Phys. G **18**, 449 (1992).
- [41] K.I. Blomqvist *et al.*, Nucl. Instrum. Meth. A **403**, 263 (1998).